ABSTRACT

Title of Dissertation:	INVESTIGATION OF CRYOGENIC SURFACE CHARGING DURING OFF-AXIS ELECTRON HOLOGRAPHY
	Kyle Anthony Sendgikoski, Doctor of Philosophy, 2022
Dissertation directed by:	Professor John P. Cumings Department of Materials Science and Engineering, University of Maryland

Cryogenic electron microscopy (cryo-EM) is an increasingly popular technique for determining the structure of solutions, especially of those with protein solutes. The ability to immobilize a fluid and attain atomic resolution of solutes within has propelled the technique to the forefront of electron microscopy. Regular advancements in resolution, specimen fabrication, data collection, and analysis mean cryo-EM will continue to expand and find new and far-reaching applications.

In this dissertation, a model system is proposed to address interface charging effects that are typically ignored when analyzing cryo-EM data. Cryogenic specimen fabrication rapidly solidifies the solution through cooling the native fluidic state, preventing short- and long-range ordering from occurring, compared to slower cooling processes. The resulting vitreous state is effectively a static representation of a liquid trapped in a solid state. In this work, cryo-EM samples are fabricated using water, and then more complex solutions, to create a baseline

understanding of the extent of surface charging from secondary electron emission. Subsequent solutions are investigated to expand the understanding of surface charging to include dispersed ions within the specimen. The interferometry technique of off-axis electron holography is used to measure the relative electron-wave phase shift produced by the specimen, which directly probes the electromagnetic fields in and around the specimen. The holography data are compared to finite-element simulations revealing that a steady-state surface charge of 1.5E-4 ± 1.6E-5 C/m^2 is generated on each surface of the vitreous solution during cryo-EM imaging. The work is repeated with a solution of functionalized Au nanoparticles roughly 30nm in diameter suspended in DI water as a model system for more complex fluids. The mean inner potential of Au nanoparticles is measured in two experiments with values of 22.3V and 22.9V and the uncertainty in both values is 2.5V from phase sensitivity. Compared with literature, these values agree with prior measurements and demonstrate cryo-EM combined with off-axis electron holography as a powerful technique to measure electric potentials in cryogenic specimens.

INVESTIGATION OF CRYOGENIC SURFACE CHARGING DURING OFF-AXIS ELECTRON HOLOGRAPHY

by

Kyle Anthony Sendgikoski

Dissertation submitted to the Faculty of the Graduate School of the
University of Maryland, College Park, in partial fulfillment
of the requirements for the degree of
Doctor of Philosophy
2022

Advisory Committee:
Professor John Cumings, Chair/Advisor
Professor Ellen Williams
Professor Lourdes Salamanca-Riba
Professor Johnpierre Paglione
Professor YuHuang Wang (Dean's Representative)

Dedication

To my parents

For my dog

For my sanity

Acknowledgements

I have debated whether or not to write this section for months. I think in time, my hindsight would look back and shake its head if I do not specify certain individuals that have been helpful in some part of this Ph. D. journey. Therefore, what follows is to assuage my future self's opinion of my current self.

The obvious I. My parents, Christine and Steven, have, let's say, encouraged me to follow what interests me. There for sure was, and still is but to a lesser extent, a dichotomy in that encouragement I received throughout my entire life but perhaps sometime in the past decade, college to now, something closer to a balance has been reached. I can enumerate specific examples where they doubted me or failed to express their opinion or pride in my chosen path. Nevertheless, they were there, they would listen (perhaps not understanding though, because who really does understand the nonsense a graduate student spits out close to a deadline), and they offered whatever assistance they could provide. If it were not for my parents, I do not know how I would have attended college, so in that way at least, they are directly responsible for enabling my self-delusions of graduate student grandeur.

The obvious II. My advisor, John, has been nearly everything I could ask for as a scientific mentor and as a person. Finding the right advisor took two pervious attempts, two years, and unfortunately, I did not learn from attempt one when looking for advisor number two. I spent most of the summer of 2018 looking for advisors doing any kind of research I was tangentially interested in…well, more so, that I didn't at first or second read find boring or ill-suited. For those that know me, the fact that I interviewed with three biology/chemistry related professors should be a shock. I think rather ironically, John actually found me more than I found him. I had reached out to John early in the summer, but because of some personal things going

on, John didn't respond until late June and basically said "you are hired if you think the project is interesting" after our first meeting. Again, I didn't practice anything I had learned from my first two advisor mishaps: I didn't talk with his current students at the time (I will mention them later). It turned out that I didn't really need to, so in the end, I finally had that ever elusive stroke of good fortune graduate students only whisper and dream about. As a graduate student advisor, John has so much to offer: deep and broad understanding of a truly surprising number of topics, willingness to answer and explain anything you might ask, patience for mistakes and poor data collection, understanding that graduate school is not the only thing in life that matters, and nuanced humor.

The obvious III. Despite John knowing many things, there are still experimental techniques he does not have actual experience with. The training I received from the AimLab staff, specifically Dr. Liou with the TEM and Dr. Chiou with cryo-EM specimen fabrication, was invaluable and greatly appreciated. As well, the training from Dr. Pozharskiy at IBBR and related conversations about cryo-EM were of equal importance and value. The staff at the FabLab were also very helpful and memorable despite not using any of the cleanroom equipment for my dissertation work. Finally, the IREAP machine shop staff and certain frequent goers I encountered are appreciated for teaching me the basics of machining. I hope to experience and learn more of this area of fabrication in the decades to come.

The obvious IV. There are a number of fellow graduate students at UMD and a then postdoctoral collaborator that were, at worst, good acquaintances through the past six years. Most graduate students will take some classes, either required or for benefit, as a first and second year student. Kaustubh W., John H., and Tsz Chun T. and myself slogged through many of those "recommended" intro courses that "prepare you" for the qualifying exams. Even though as time

passed and our individual research occupied more of our time, we continued to commiserate the struggle of our common [graduate students] and provide insight and alternate scientific challenges on a consistent basis. Through the funding for my dissertation research, I collaborated with a group at MIT and met Matthias K., a postdoc aus Deutschland. Matthias is a great scientist, collaborator, and "workplace proximity acquaintance." Finally, Hsin-Yun (Joy) C. and Zoey W., former Cumings' graduate students, have been tremendous friends since I met them. They were a source of great laughs and practical scientific suggestions.

Some other people.

That one person that will remain nameless for …. ah f@k it*. I knew someone from sometime in college to nearly the end of graduate school. They were there for everything I struggled through as I got my Ph. D., perhaps not in the best ways at times, but always trying to be positive and supportive. They deserve at least briefly tacit, but fully begrudged, recognition for the security and tireless sounding board they provided. (what a bi!*h)

Possibly the most important people for my sanity. Those that know be better than most others know that there are a few select things I will sacrifice anything for. One of those is playing basketball twice a week at 6am. When I started graduate school, I would go to the gym most every morning and workout. After a while, my itch to play basketball was enough to shot hoops by myself. Thankfully I did this in the morning on the same side as a group of older, and some younger, basketball players who needed a tenth player. From that random day onwards, morning basketball with Dre, Chuck, Chico, Tom, Steve, and as time passed other random undergraduate and graduate students (John, Ben, Rainer, Evan 1, Evan 2, Sam, and some others I am forgetting), has been a truly cathartic and healing time for me. Something else that those who know me best also know is that I used to play an online game rather consistently for the past 7

years (recently I have stopped because of this cursed document). I met two people, Pedro and Xavi, in that game and we have had countless laughs, arguments, banter, and fun since. I truly appreciate the joy and lightheartedness (and sometime depressive overhanded conversations) that emerged from the people I mentioned in this paragraph.

The last two and two. I have learned a lot as I passed through graduate school. One of my key takeaways is that just like athletes hire a trainer and chef to improve their bodies, every person on the planet should talk with a therapist at least a few times initially and every once in a while thereafter because no one has it fully together, is harboring zero past trauma, and is not in need of internal and mental growth. My first therapist was amazing and truly opened my eyes to the absolute annoyance society dictates everyone conform to…as well as point out why we probably should try to conform a bit. My current therapist has challenged me in almost every conversation we have, constantly pushing me to think of different perspectives and outcomes. Thank you. Two other thankless entities these past years have been Glenmark Pharmaceuticals and Shire Products that without, this document might not exist.

My posterity assuaged, I conclude with a thank you that will never be known.

Thank you Avery.

Table of Contents

List of Tables

List of Figures

List of Abbreviations

TEM-transmission electron microscope

a-C-amorphous Carbon

MIP-mean inner potential

FOV-field of view

PLA-projector lens aperture

CL3-condenser lens 3

psf-point spread function

LDA-low density amorphous

FLC-free lens control

SA-selective area

DI-deionized

3-MPA-3 mercaptopropionic acid

LN-liquid nitrogen

DM-Digital Micrograph

TIE-transport of intensity equation

PUA-phase unwrapping algorithm

PB-Poisson Boltzmann

tds-Transport of Dilute Species

PNP-Poisson Nernst Planck

List of Variables

m_e-electron mass

q_{max}- maximum spatial frequency recorded

J_0- mean current density

A- amplitude

C- fringe visibility/contrast

C_{inst}-TEM instabilities

C_{MTF}-modulation transfer function of the CCD

C_{inel}-inelastic interaction with the object

q_c- spatial frequency

φ- phase

v_b- minimum variance bound for estimation of spatial frequency/amplitude/

N-electron number

$\tilde{V}$-reduced fringe visibility

$\tilde{N}$-reduced electron number

STE(q)-signal transfer efficiency

SNR_{out}-signal to noise ratio of the output of the image detector as a function of spatial frequency

SNR_{in}- signal to noise ratio of the input of the image detector as a function of spatial frequency

ξ, η-elliptical semi-major/minor directions

β-mutual angular distance

a-distance from the biprism to the source

b- distance from the biprism to the interference plane

r_G-Gaussian radius

I-electron current

B-brightness of electron radiation

A_1-area electrons emitted into

Ω-solid angle

Chapter 1: Introduction

1.1 Confined Fluids

The ability to contain water in a vessel that does not leak has been a prominent focus and requirement for humans' survival throughout history. The survival of life itself is predicated on a person's ability to have access to water and the ability of a person's body to retain the water for a reasonable period of time. Just like the first gourds used to retain water, cells are tasked by the body to retain that same water to maintain function. As time has passed and the focus of every human shifted from survival to investigation, improvements in water storage, transport, and cleaning became an increased focus until water was an overlooked, but vital resource taken for granted (ignoring obvious cases where water scarcity or contamination have been a concern such as following a civil or natural disaster). The implementation of confined water dates back to Mesopotamia around 4000 B.C.E[1]. It took humans over 5000 years to understand mathematically how those original pipes worked with Bernoulli's *Hydrodynamica*[2] in 1738 and another 200 plus years to study confined liquids at submicron length scales.

The sheer magnitude of fluid confinement-based effects at play in everyday life has few parallels. At its core, when a volume of fluid passes through a confined space, filtration is occurring if separation of constituent components results. Understanding the effect pore size has on selectivity, transport, and longevity will lead to new and improved filtration technologies[3]. One key way to understand the importance of this is to look at the global fresh water supply and the demands on it. Population growth and industrial expansion continually increase the demand for clean water and energy[4–6]. Water desalination can reduce the stress on natural freshwater

supplies but the process is energy intensive in its current form[5]. Improving desalination requires highly selective and permeable membranes[7,8] as well as reduction in post-separation steps[9,10]. Custom designed membranes are needed to achieve these improvements, for which a better understanding of confinement effects is necessary[3,10]. Because increasing confinement leads to a breakdown in the classical descriptions of fluid behavior, continued research at high resolutions and advanced modeling is needed to find accurate descriptions of these systems. Example systems including carbon nanotubes[11–13], boron nitride nanotubes[14], graphene oxide laminates[15,16], and polymer[17,18] and silicon[19,20] nanochannels have been probed with spectroscopies[21–27], simulations[28–30] and models[31–37] to understand solvation[29,30] and selectivity[38]. However, many of these techniques do not have the ability to probe spatial distributions, just how a parameter is changing. The ability of electron microscopy to capture the physical system at high resolution and small length scales in the form of an image and provide specimen parameters situates electron microscopy as an optimal characterization technique.

1.2 Electron Microscopy

The ability to look at smaller and smaller things has allowed for ever greater levels of detail and description. From the initial discoveries afforded by optical microscopes[39] to the more recent transmission electron microscope (TEM) proposed by Knoll and Ruska[40,41] made possible by electromagnetic lens proposed by Busch[42], the ability to “Gaze into the abyss” and report with ever improving accuracy has made for prolific discoveries.

Within a year of the first TEM being built, the optical resolution limit from de Broglie was surpassed with a TEM[43]. As decades passed from the late 1930s with the first commercial TEMs, steady and continued improvements allowed for broader applications with an increased

level of detail. More powerful, coherent, and stable electron emitters enabled higher resolution, higher magnification, and broader specimen applicability. Similarly, improved multipole electron optics significantly advanced the capabilities of a TEM, most notably with the more recent development and accessibility of spherical aberration correction. Thinner “foils”, originally pertaining to metal films thinned from bulk, and electron diffraction developed by Hirsch, further advanced the field of electron microscopy[43]. Electron detection systems have seen significant recent advancement from photographic film to CCD and now direct detection systems that are capable of counting individual electrons. Another advancement occurred with the improvement of semiconductor transistors: computer controlled TEMs.

Coinciding with the continued advancements of the TEM itself are the development of techniques such as diffraction, electron energy loss spectroscopy, energy dispersive x-ray spectroscopy, scanning TEM, high-resolution TEM, dark field TEM, holography, and ptychography as well as a variety of in-situ TEM holder capabilities. Each technique has its own specific use cases and specialized applications that can assist other techniques both inside and outside a TEM. With improvements to specimen holders and additions to the electron microscope itself[44–48], the range of possible experiments continually expands. Heated specimens[49], atomic columns[50–52], cryogenic specimens[53–56], liquids[57–63], nanotubes[64–67], and batteries[67–69] have all been probed with an electron microscope. The ability not only to see what is happening but also to gather physical properties in parallel affords the electron microscope a prime spot in the materials investigation toolbox.

Of all the capabilities of a modern TEM, electron detectors can only record the amplitude of the incident electrons—their probability to arrive at a point in space at a given time. The phase

information is nearly always ignored, forgotten, or inaccessible. The most common imaging mode in a TEM is amplitude contrast, mainly composed of mass-thickness and diffraction contrast. Mass-thickness contrast arises from variations in the density and/or the thickness of the specimen and is described by Rutherford scattering. Diffraction contrast is the result of Bragg diffraction from a crystalline structure and, when present, can dominate the amplitude signal over mass-thickness.

Another contrast method is termed phase contrast such as Fresnel, atomic resolution, and Zernike[70]. The dominant form of phase contrast results from specimen crystal planes splitting the incident beam into transmitted and scattered beams that differ in their phase by an amount proportional to the lattice spacing. The two beams are overlapped by the objective lens resulting in an interference pattern at the detector, again proportional to the lattice spacing, resulting in an atomic resolution image. Unfortunately, the phase information is not directly recorded, and few TEM techniques exist that enable extraction of the phase of the transmitted wave. Chapter 2 begins with a discussion on a TEM technique that allows the phase of the electron wave to be encoded into the recorded amplitude signal: electron holography.

The high spatial resolution afforded by a TEM makes studying nanotubes and nanoparticles a preferred system to gain information on ionic solvation and transport at the interfaces and within nanotubes. The technique of off-axis electron holography, described in detail in chapter 2, is an interferometry technique that allows measurement of the electromagnetic properties of a specimen. Successful use has been seen in measuring mean inner potentials[71–77], stray electric fields around microparticles[78], native, unstrained structures in biology and chemistry[79,80], semiconductor interface potentials[81–83], grain boundary potentials[84],

and ferroelectric polarization[84–86]. Implementing off-axis holography in a TEM could potentially illuminate missing understanding of ion solvation and charging effects. Specifically, specimen charging under electron irradiation can produce spurious phase variations and is often ignored in other cryo-EM systems that cannot otherwise reveal the surface charge or shifted phase of the electrons[87–89].

1.3 Experimental Goals

With the use of an electron microscope equipped with a Möllenstedt[48] biprism and the fabrication technique of cryo-EM specimens, electrostatic potentials inside and outside cryogenic specimens are studied. The practical implementation and fundamental limitations of off-axis electron holography with cryo-EM specimens are explored. The occurrence of specimen charging during cryo-EM is studied and quantified. Nanoscale solvation at a charged interface is modeled and length scales accessible by holography are estimated. The observed specimen solutions and measurement sensitivities resolved the mean inner potential of the solute. As a result, an understanding is achieved of experimental capabilities, improvements are outlined, and future opportunities for specimen configuration and measurement goals are discussed.

1.4 Structure of this Dissertation

The four remaining chapters of this dissertation address the following topics. Chapter 2 introduces the foundations of off-axis electron holography, outlining the physics of hologram formation, the acquisition of an electron hologram, the impact of hologram parameters on the sensitivity and spatial resolution, and the fabrication of cryo-EM specimens. Chapter 3 presents the method of electron hologram analysis and the model used to compare holograms to

experimental data. Chapter 4 moves forward with implementing the analysis and model of chapter 3 on the acquired holograms and providing an interpretation of the results. Chapter 5 concludes this Dissertation with a summary of the results and outlines future opportunities for the combination of cryo-EM and off-axis electron holography.

Chapter 2: Electron Holography

2.1 Physics and Operation

Standard amplitude and phase contrast TEM imaging provides interpretable information related to the amplitude. The phase information remains inaccessible because the detector only records electron count intensity that is directly related to the amplitude of the propagating electron wave. The inability of the detector to record the electron phase in an independent or separable way from the amplitude requires encoding of the phase information with some amplitude-dependent mechanism. This encoding is achieved by creating interference in the electron wave after the specimen resulting in interference fringes that the detector records as a variation in the amplitude. With the phase information encoded into the amplitude, post processing of the electron micrograph can separate the pure amplitude and phase information of the original image. This now accessible and often forgotten phase information is directly related to the electromagnetic fields of the specimen and provides significant insight into specimen properties that otherwise could be inaccessible.

2.1.1 Electron Holography

The original electron-optical holography work proposed by Gabor[90–92], creating a "projection method"[93] where the entire optical system was located between the light source and specimen, was quickly modified by Haine and Dyson[94] moving the optics between the specimen and the detector, then a photographic plate, creating the "transmission method." This original interferometry setup, now termed in-line to describe the path electrons follow, suffered from 'conjugate' twin images that can be minimized by staying in the Fraunhofer condition, resulting

in a significantly spread conjugate image[95]. The in-line technique is more often superseded by the off-axis technique, but still finds use in measurement of boundary and interface structures and composition[96], as an alternative to confocal microscopy in biological endeavors[97,98], the study of liquid and flow propterites[99,100], and the foundation for ptychography[101]. Since the original discovery of optical holography by Gabor, there have been numerous proposed holography techniques[102] of which, the following discussion focuses on the primary method of off-axis holography.

For several decades, off-axis holography was minimally used from its original demonstration by Leith and Upatnieks in 1962[103], but with the advent of stable coherent field emission electron guns in commercial TEMs, the technique became significantly more prevalent[104]. Off-axis electron holography allows for the separation and independent interpretation of both the amplitude and phase of an image[71] with the phase being directly related to the electromagnetic field of the specimen. To achieve this separation, the electron wave typically passes through the material specimen and an adjacent empty vacuum space in the same plane, creating a specimen wave and reference wave, respectively. The term “off-axis” comes from the effective two electron paths created in the microscope. An alternative condition, termed “difference holography,"[104,105] can be achieved by replacing the vacuum space with a section of the specimen with known properties.

In Figure 2.1A, the specimen wave is shown in blue only after the electron wave passes through the specimen. The reference wave is shown as empty white space after the specimen. Both specimen and reference waves pass through identical electron optics in the TEM. Then the two waves pass either side of the electron biprism[48,106,107], a conducting wire of sub-micron

diameter. A modern electron biprism is made by pulling a quartz fiber to a diameter of 1μm or less using a hydrogen torch[108,109]. The fine quartz fiber is coated in a metal, typically Au or Pt, and mounted on a stage allowing for an applied voltage to the biprism. As an aside, work has been done to create lensless interferometers and biprisms made of carbon nanotubes[110–112]. The voltage on the biprism alters the trajectory of the passing electron wave so that the specimen and reference waves overlap after the biprism creating an interference pattern shown as the orange line at the detector in Figure 2.1A. The difference in the electron path length, or more precisely, the relative phase difference the electrons gain along their trajectory, is encoded in the interference pattern in the amplitude at the detector.

Figure 2.1

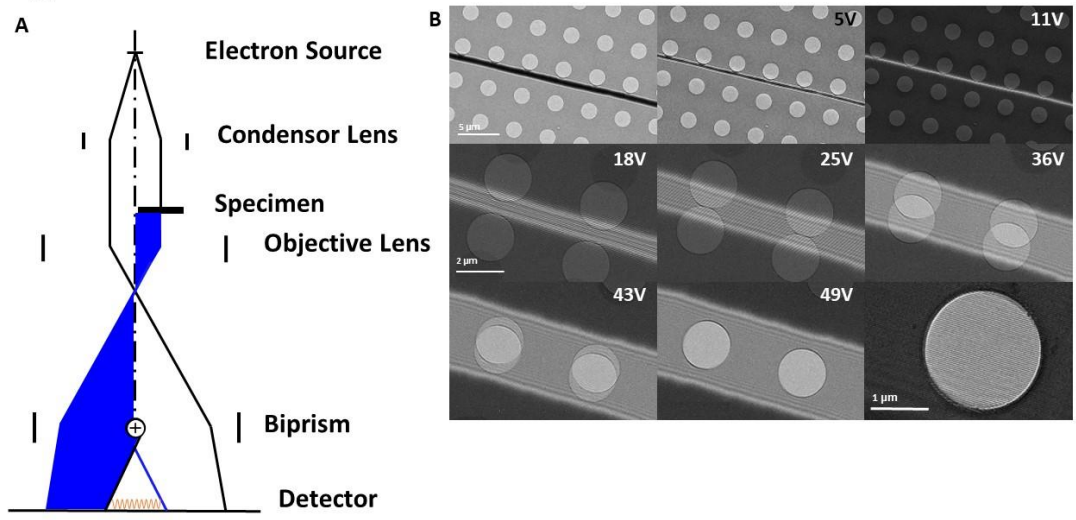

Figure 2.1: A schematic diagram of a TEM in off-axis holography mode (A), where the electron biprism is inserted into the column and a bias voltage is applied resulting in an interference pattern at the detector. The blue region depicts the electron wave that has passed through the specimen and the complimenting white region is the reference wave that only passes through vacuum. An array of electron holograms collected at 1kX and 3kX magnification (B)(top row and bottom two rows respectively) where the biprism bias has been varied from zero to 49V. The final image at the bottom right is a representative hologram to better show the interference fringes. All holes have a diameter of 2μm.

As the biprism voltage is increased, the extent of the overlapping specimen and reference waves increases as shown in Figure 2.1B. There is both an upper and lower bound on the amount of applied voltage that produces a reasonable hologram. When the biprism voltage is too low, there is either no overlap of the two waves or the overlap produces insufficient fringe density, fringe width, and contrast depicted in the first row of Figure 2.1B. Increasing the biprism voltage above a value defined by the specimen geometry and electron beam coherence results in the loss of optical coherence between the two waves reducing the contrast of the interference at the detector. Figure 2.1B displays a series of consecutively captured images where the electron biprism voltage spans from 0V to 49V on an empty Quantifoil TEM grid. Quantifoil is a periodic array of uniformly spaced and sized holes on an amorphous carbon (a-C) film supported by a metallic TEM grid. The first row of images was taken at 1kX effective magnification and an acquisition time of 2s. The last two rows were taken at an effective magnification of 3kX and acquired over an 8s exposure. At 11V, the two opposing edges of the biprism are just beginning to overlap and as the voltage increases to 49V, enough so that neighboring holes perfectly overlap, interference fringe density is increased. The resulting interference/fringe pattern, called an electron hologram, from the wave overlap is a combination of Fresnel contrast and interference fringes recorded at the detector. The bottom right image in Figure 2.1B is from a different specimen but is a representative hologram depicting the fringe pattern in greater detail.

Positioning of the electron biprism in the electron column[107], the biprism orientation relative to the specimen, the beam coherence, and the interference pattern at the detector are all significant in acquiring a high-quality electron hologram. The biprism is suspended on a 360° rotational stage co-axial to the electron beam allowing for any desired orientation of the biprism

to the specimen. The biprism is electrically biased through an external power supply with a range from 0 to 316V with a precision of 0.1V. Contamination and distortion of the biprism does occur over time because the vacuum is not perfect, the applied voltage on the biprism can attract debris, and the electron beam can damage the biprism. The result of contamination is a non-uniform hologram, therefore finding a clean, straight section of the biprism is done through the in-plane translation control. Rotational control of the biprism is done through the power supply and in-plane translation is done through a manually operated knobs on the biprism housing. The biprism is located below the objective lens and nearly co-planar to the selected area aperture in the JEOL 2100F FEG TEM used for this work. The location of the biprism results in the interference pattern forming in the final projected image.

2.1.2 Hologram Phase

Understanding where the phase that electron holography records originates from is equally important to the mathematical description of that phase[113]. Consider the exit wave transmitted through the specimen

$$\Psi(\boldsymbol{r}) = \Psi_K(z)\Psi_0(x,y) = e^{2\pi iKz}a(x,y)e^{i\phi(x,y)} \tag{2.1}$$

where Ψ_K is a monochromatic plane wave incident on the specimen, Ψ_0 is the input signal of the microscope, commonly called the information channel, and K defined by $(\hbar K)^2 = 2m_e U^*$ with U^* being the relativistic corrected accelerating voltage. Inserting equation 2.1 into the relativistically corrected time-independent Schrodinger equation (being the same as the spinless, scalar Dirac equation in the lab frame)

$$\frac{1}{2m_e}(-i\hbar\nabla + e\boldsymbol{A})^2\Psi(\boldsymbol{r}) = e[U^* + \gamma V(\boldsymbol{r})]\Psi(\boldsymbol{r}), \tag{2.2}$$

which yields the phase shift based on the Aharonov-Bohm effect[114],

$$\phi(x,y) = \frac{\pi\gamma}{\lambda U^*}\int V(x,y,z)dz - \frac{e}{\hbar}\int A_z(x,y,z)\,dz, \tag{2.3}$$

where $\gamma = 1 + eU/m_e c^2$ is the relativistic Lorentz factor, $\lambda = h/\sqrt{2em_e U^*}$ is the electron wavelength, and $U^* = U(1+\gamma)/2$.

For equations 2.1 and 2.2 to result in 2.3, the Eikonal approximation is used, and the problem is treated semi-classically by looking for a solution with an amplitude, phase, and monochromatic temporal dependence. The Eikonal approximation is generally valid when the spatial variation of the electron wave amplitude is long compared to the electron wavelength[113]. An appropriate gauge is chosen but different authors use different gauges and disputes over gauge invariance remains the norm[113]. Rewriting equation 2.3 into a more familiar form yields

$$\Delta\phi(x,y) = C_E\int V(x,y,z)dz - \frac{e}{\hbar}\iint \vec{B}(x,y)\cdot d\vec{S} \tag{2.4}$$

where $C_E = 7.29\,mrad/Vnm$ is the electrostatic constant at 200kV. The form of equation 2.4 is used by most authors of electron holography theory.

When the specimen is non-magnetic, equation 2.4 becomes

$$\Delta\phi(x,y) = C_E\int V(x,y,z)dz \tag{2.5}$$

and is the primary equation this dissertation is based on. The composition of potential V in equation 2.5 includes both the long-range charge distribution and electrostatic potentials within the constituent atoms of the specimen, the latter of which has a spatial average called the mean inner potential (MIP)[71].

2.1.3 Acquiring an Electron Hologram

Consideration here is given solely to acquisition of an off-axis TEM hologram. Specimen fabrication will be discussed later in this chapter. The desired specimen is inserted into a highly coherent FEG TEM equipped with a sufficient electron biprism and digital CCD camera. After specimen insertion, Holography mode is engaged providing access to the predetermined lens relationships necessary to acquire an electron hologram. Holography mode enables the electron lenses to form a magnified specimen image near, but not directly at, the biprism plane. The desired final magnification is selected via the intermediate lenses with ranges and camera field of view (FOV) values given in Table 2.1. Holography FOV is discussed in section 2.1.4.3. When a desired magnification range is selected, primary focusing of the beam is controlled with the Objective Focus knob typically to a large, positive value. Just as in mass and phase contrast TEM mode, further refinement of the beam is done at higher magnifications than the intended imaging magnification if possible. Focus, objective astigmatism, intermediate astigmatism, and voltage (or current) centering are done in an identical manner to TEM mode, typically recursively. Occasionally the projector lens aperture (PLA) shift is needed when beam centering cannot be achieved with condenser aperture and beam shift manipulation.

Standard TEM mode has a defined 'optimal' defocus condition called Scherzer defocus[115] defined as

$$d_{Sch} = -1.2\sqrt{C_s/k} \tag{2.6}$$

where $C_s$is the spherical aberration coefficient and $k = 1/\lambda$ is the wave number. For typical C_s, $d_{Sch} = -68nm$ for 200keV electrons. Scherzer defocus aims to minimize the number of zeros in the contrast transfer function while extending the first zero as far from the origin as possible. The

Gabor defocus for medium resolution applications is defined as $d_{Gab} = -0.67\sqrt{C_s/k} = 0.56d_{Sch}$, and it aims to minimize cross talk between the amplitude and phase[116,117]. For high resolution applications where the coherent wave aberration is corrected, the optimal defocus for holography

$$d_{z,opt} = -0.75C_s\left(\frac{q_{max}}{k}\right)^2 \quad (2.7)$$

aims to collect the maximum amount of retrievable phase information from the object[117] and is 2-3 times d_{Sch}, where q_{max} is the desired spatial frequency.

Mode	**Panel setting**	**Magnification range**	**Camera FOV** (μm)
Holo-L	Low Mag	1k-6k	50.0 – 8.88
Holo-M	Mag 1	100k-300k	1.18 - 0.86
Holo-H	Mag 1	300k+	< 0.86

Table 2.1: Magnification and field of view for the three built-in holography modes are given.

After the specimen and beam are at satisfactory conditions, the electron biprism is inserted at zero applied bias. The biprism is located with use of the in-plane translation stage knobs and aligned to the specimen with the rotational controls on the power supply. A desired bias is applied to the biprism creating the interference pattern and the electron hologram is recorded with the camera. Adjustment of condenser lens 3 (CL3) is used to move beam crossover below the sample plane such that the incident beam is highly parallel at the sample plane. This CL3 adjustment is often called beam spread. The result of moving condenser crossover below the sample plane is an increase in beam collimation at the cost of electron intensity. Following sections in this chapter will further discuss beam conditions, holography sensitivity, and specimen fabrication.

2.1.4 Parameter Effects on Holography and Analysis

Acquiring a high-quality electron hologram encompasses the same image properties as standard TEM such as focus, astigmatism, drift, contrast, detector quality, magnification, and various resolutions. Specimen properties such as thickness, thickness variation, geometry, and composition affect transmitted and scattered electrons as well as the interpretation. There are additional properties that impact the quality of an electron hologram in ways beyond standard TEM: fringe spacing, fringe contrast, pixel size, and electron counts. Fringe spacing is primarily controlled by the magnification and the biprism voltage. Fringe contrast is strongly affected by beam coherence, pixel size (by magnification), and electron counts (by exposure time, which is also closely linked to stage drift). However, these holography specific properties are not solely controlled and uniquely independent of other TEM parameters, just as in standard TEM mode. To facilitate an understanding of how these properties are linked and where the fundamental limitations lay, a discussion of holography limitations follows based on the work of Harscher and Lichte[118–122].

Starting[123] with a coherent TEM image, the image electron wavefunction is

$$\psi_i(\boldsymbol{r}) = A_i(\boldsymbol{r})\exp\left(i\phi_i(\boldsymbol{r})\right) \tag{2.8}$$

with a two-dimensional vector in the sample plane **r**, with A_i and $\phi_i$in the image plane both denoted by subscript i. An off-axis hologram wavefunction, in the biprism overlap region at the image plane, is the sum of the initial specimen wave in equation 2.8 and a tilted reference plane wave resulting in

$$\psi_i(\boldsymbol{r}) = A_i(\boldsymbol{r})\exp\left(i\phi_i(\boldsymbol{r})\right) + exp(2\pi i\boldsymbol{q}_c\boldsymbol{r}) \tag{2.9}$$

The recorded intensity distribution is given by

$$I_{hol}(\boldsymbol{r}) = |\psi_i(\boldsymbol{r})|^2 \quad (2.10)$$

$$= 1 + A_i^2(\boldsymbol{r}) + 2A_i(\boldsymbol{r})cos[2\pi i \boldsymbol{q}_c \boldsymbol{r} + \boldsymbol{\phi_i}(\boldsymbol{r})] \quad (2.11)$$

where $\mathbf{q}_c$ is the two-dimensional tilt of the reference wave. The intensity as shown in equation 2.11 has a sum with three terms: (1) the reference wave, (2) the image wave, (3) and a set of cosinusoidal fringes with local phase shifts and amplitudes.

Recasting equation 2.11 from intensity to current density gives

$$j(x, y) = \frac{j_0}{2}[1 + A^2 + 2AC\cos(2\pi q_c x + \phi)] \quad (2.12)$$

where the interference fringes are parallel to the y-axis, and the amplitude and phase of the image wave are assumed constant over the entirety of the hologram. The fringe visibility or contrast, C, is

$$C = \frac{I_{max} - I_{min}}{I_{max} + I_{min}} = |\mu| C_{inst} C_{MTF} C_{inel} \quad (2.13)$$

where I_{min} and I_{max} are the minimum and maximum of intensity and, μ the spatial coherence, is introduced in section 2.1.4.2. The instrumental contrast C_{inst} accounts for all the microscope instabilities, and the camera contrast C_{MTF} accounts for the modulation transfer function of the detector. The inelastic contrast $C_{inel} = e^{-d/2\lambda_{inel}}$ roughly accounts for inelastic interactions with the specimen. The first expression in 2.13 is the empirical formula and the second expression is a model of source contributions to decoherence.

2.1.4.1 Detection Limits

The composition of noise in an electron hologram comes from electron shot noise and other instrument related sources. Considering a finite number of electrons, the standard deviation for phase detection is given by

$$\sigma_\phi = \sqrt{\frac{2v_b}{C^2 N}} \tag{2.14}$$

and a phase signal-to-noise ratio given by

$$SNR_\phi = \frac{\phi}{\sigma_\phi} = \phi C\sqrt{\frac{N}{2}} \tag{2.15}$$

where v_b is the minimum variance bound and a detailed discussion can be found in Appendix A of reference 94. The minimum variance bound is set to one because the spatial frequency and direction of interference fringes are known[120,124]. The minimum detectable phase difference between two neighboring pixels is a rearrangement of equation 2.15 giving

$$\delta\varphi_{lim} = \frac{SNR_\varphi}{C}\sqrt{\frac{2}{N}} \tag{2.16}$$

with units of radians and a standard minimum $SNR_\varphi = 3$. The definition of N is "the electron number collected in the hologram per subsequently reconstructed pixel"[118] and very important when following the analysis in chapters 3 and 4. As a brief example, with C = 0.2 and N = 100 or 1000, $\delta\varphi_{lim}$ = 2.1213 or 0.6708 radians respectively.

The measurement precision of the fringe visibility is[120]

$$\sigma_V = \sqrt{\frac{2-C^2}{N}}. \tag{2.17}$$

The standard deviation of the amplitude is calculated by expressing the amplitude of the reconstructed wave as $A = CN$ and applying the law of error propagation where a Poisson distribution is assumed for electrons with $\sigma_N = \sqrt{N}$ resulting in

$$\sigma_A = \sqrt{{\sigma_V}^2 N^2 + C^2 {\sigma_N}^2} = \sqrt{2N}. \tag{2.18}$$

Using the result from equation 2.18, the SNR for the amplitude in the image plane is [124]

$$SNR_A = \frac{A}{\sigma_A} = C\sqrt{\frac{N}{2}} = \frac{1}{\sigma_\varphi}. \quad (2.19)$$

To account for any alterations of the electron beam from the specimen in relation to the incident wave, for example due to inelastic scattering, an amplitude difference a results from electron count loss and/or a reduction in fringe contrast in the reconstructed wave

$$a = CN - \tilde{C}\tilde{N}. \quad (2.20)$$

Therefore, the adjusted amplitude SNR now becomes

$$SNR_a = \frac{a}{\sigma_a} = \frac{CN - \tilde{C}\tilde{N}}{\sqrt{2(N+\tilde{N})}} = \zeta\frac{C\sqrt{N}}{2} \quad (2.21)$$

where $\zeta = 1 - \tilde{C}\tilde{N}/CN$ which is a measure of amplitude contrast. When the reduction in fringe contrast is ignored (i.e. $C = \tilde{C}$), $SNR_a = \zeta\, C\sqrt{N}/2$ for weak phase specimens where $\zeta \ll 1$. A similar result occurs when the damping of the wave is ignored: $N = \tilde{N}$.

The addition of the detector influence can be added to extend the description of detection limits to be more complete. The detector influence, characterized by signal transfer efficiency (STE), for slow-scan CCD electron microscopy cameras[125] is given as a function of spatial frequency q as

$$STE(q) = \frac{SNR_{out}(q)}{SNR_{in}(q)} \quad (2.22)$$

where SNR for the CCD is defined as the ratio of power of the signal to that of the noise. This signal transfer efficiency inserts as a multiplicative corrective factor for SNR_A in equation 2.19 resulting in

$$SNR_A = \sqrt{STE(q_c)}\sqrt{\frac{C^2N}{2}}. \quad (2.23)$$

Given the definition in equation 2.16, a confounding discrepancy occurs when trying to determine what is meant by "phase detection limit" and SNR. On one hand, minimizing the phase detection limit implies that a smaller value is good but on the other side of 2.16, a low SNR is bad. The common practice appears to be intentionally setting SNR = 3, and using C, N from the measured hologram to determine the phase detection limit from the model. For this reason, and because 2.15 and 2.16 are interdependent, 2.14 is used to calculate the sensitivity of the hologram in chapters 3 and 4. Equation 2.16 appears to be a measure of the ideal, absolute minimum detectable phase shift and not the actual phase measurement sensitivity.

2.1.4.2 Fringe Visibility

The optimum fringe contrast, C, starts with circular, or more generally elliptical, condenser illumination with normalized current density

$$i(\xi,\eta) = \frac{1}{\pi r_\xi r_\eta} exp\left(-\left(\frac{\xi^2}{r_\xi{}^2} + \frac{\eta^2}{r_\eta{}^2}\right)\right) \tag{2.24}$$

when the biprism is parallel to η-axis, the degree of spatial coherence, μ, perpendicular to the biprism between two points in the hologram plane as seen from the source plane is

$$\mu(\alpha, r_\xi) = exp\left(-(\pi k\beta r_\xi)^2\right) = exp\left(-\left(\pi r_\xi \frac{1}{s}\frac{b}{a}\right)^2\right) \tag{2.25}$$

where $s = b/ak\beta$ is the spacing of the interference fringes. Equation 2.25 is the Fourier transform of 2.24 by use of the Van Cittert-Zernike Theorem[126]. The primary advantage of elliptical illumination is the mean current density increasing by $\epsilon = r_\eta/r_\xi$, without decreasing coherence, and fewer beam parameters to optimize during alignment.

With the phase detection limit and fringe contrast described, electron counts, fringe spacing, and pixel size remain. Electron counts and fringe spacing are linked through the lateral

resolution which is governed by the information limit of the microscope. Pixel size and electron counts are linked through coherent current density, field of view, and the CCD. Each of these will be addressed individually.

2.1.4.3 Field of View, Lateral Resolution, and Pixel Number

The holography FOV is determined by the hologram width which is controlled by the diameter of the biprism image and the applied biprism voltage. The closer crossover is to the biprism, the lager the biprism appears at the detector. Optimizing the width of the biprism to encompass as large an area as possible runs counter to optimizing collectable electron dose, which is achieved by decreasing the size of the biprism. A minimum voltage is required to overcome the width of the biprism image, causing initial overlap of the specimen and reference wave. Further increasing the voltage increases the FOV and simultaneously decreases fringe spacing, but also decreases contrast. At lower resolutions and magnifications, the FOV has a wide range of values (μm range), if the object detail is consistent with the spatial resolution. As resolution and magnification requirements increase, aberrations become more impactful, so the FOV should be at least four times the point spread function (psf) given by

$$psf = 0.5C_s\left(\frac{q_{max}}{k}\right)^3, \tag{2.26}$$

to gather the intended information. Equation 2.26 is the smallest value at $d_{z,opt}$ but thankfully, C_s correction reduces the psf below the lateral resolution, when it is available.

The lateral resolution of high-resolution TEM is limited by spherical and chromatic aberration of the objective lens. Before practical aberration corrected electron lenses, the holographic method was proposed as a way to circumvent image degradation from lens

aberrations[92,127]. In a hologram, the fringe spacing determines the reconstructable lateral resolution q_{res}. For a strong phase object, the carrier frequency must satisfy $q_c \geq 3q_{res}$ to fully mask the sideband from the centerband. Or more simply, three fringes are required to sample a reconstructed period. This three-fringe requirement is relaxed to 1 fringe for weak phase objects. Often there is no benefit going past the one or three fringe requirement because the CCD has a limited number of pixels and fringe contrast inevitably becomes more challenging.

Just as there is a requirement on the number of fringes to sample an object, there is also a requirement on the number of pixels that sample each fringe. If sampled above the Nyquist frequency, there will be no loss of information. Each holographic fringe should be sampled by between 3-5 pixels of the detector[118,124,128]. Choosing a four-pixel requirement and combining with the requirement for object fringe number, the following equation for detector pixels that limits reconstructable pixels is

$$n_{rec} = {}^{n_{pix}}/_{g} \tag{2.27}$$

where g is 12, 4 for strong and weak phase objects, respectively. This means that a strong phase object requires 12 detector pixels for every one reconstructed pixel in the phase map.

2.1.4.4 Current Density and the Detector

In equation 2.13, the total coherence $|\mu|$ is composed of spatial and temporal coherence. When the fringe number is <1000, temporal coherence is a nearly zero correction to spatial coherence defined in equation 2.25[118]. In standard TEM mode, the diameter of the psf≈$5d_{Sch}$ must be illuminated coherently. In holography, under elliptical illumination, the coherent region of illumination is significantly greater. Because the strength of coherence significantly impacts

fringe contrast, consider the following comparison between coherent current and coherent current density.

Consider a Gaussian illumination source given by

$$\boldsymbol{i}(r_s) = \frac{1}{\pi {r_G}^2} exp\left(\left({r_s}/{r_G}\right)^2\right) \quad (2.28)$$

with a degree of coherence

$$\mu^{sc}(\alpha) = exp(-(\pi k \alpha {r_G}^2)^2). \quad (2.29)$$

Using the axial brightness of electron radiation

$$B = \frac{I}{A_1 \Omega} = \frac{I}{(\pi r_G \alpha)^2} \quad (2.30)$$

where $A_1 = \pi r_G^2$ and $\Omega = \pi \alpha^2$, the coherent current emitted into a coherently illuminated cone is

$$I_{coh}(|\mu^{sc}|) = -\frac{B}{k^2} log(|\mu^{sc}|). \quad (2.31)$$

Given equation 2.31, the following two observations can be made. First, when $\mu^{sc} \approx 0$ there is zero contrast but many electrons as $-log() \rightarrow \infty$, and secondly, when $\mu^{SC} \approx 1$ there is maximal contrast but zero electrons as $-log() \rightarrow 0$. Optimizing the coherence results in $\mu^{SC} = exp(-1/2) \approx 0.61$. This results from B/k^2 being independent from the accelerating voltage so I_{coh} is a property of the emitter. However, the coherent current density can be optimized for holography with an elliptical profile. With elliptical illumination, coherence parallel to the fringes can be less than the coherence requirement perpendicular to the fringes (i.e. perpendicular to the biprism)[48,118].

2.1.4.5 Specimen Properties

Like other electron microscopy techniques, specimen properties directly impact the ability to collect data, the quality of the data, and the interpretation of the data. Not only does

specimen thickness and composition affect the reconstructed phase, but the geometry does also as well. Specimen geometry is possibly the most important property that affects holography. If the specimen does not allow for vacuum-specimen overlap or the aforementioned "difference" holography condition cannot be implemented, then there is no option for off-axis holography. As mentioned, the most common holography method of vacuum-specimen overlap requires the area of interest on the specimen to be in 'close' proximity to an area that has no specimen, that is, just vacuum. The definition of close depends on, in order of importance, beam coherence, the overall ability of the electron optics to focus and correct any astigmatism, and magnification.

The ideal specimen thickness d can be calculated by optimizing the acquired phase shift against the loss of coherence due to inelastic scattering,

$$dC_{inel} = de^{-d/2\lambda_{inel}}, \tag{2.32}$$

with optimum thickness occurring at $d = 2\lambda_{inel}$. Equation 2.32 comes from writing the differential infinitesimal of equation 2.5 as $\delta\phi = C_E d\delta V$ assuming the potential does not vary in z and rewriting $\delta\phi \propto 1/C_{inel}$[118].

Later in section 2.2, specimen fabrication is discussed including cryogenic vitrification of water which produces a low density amorphous (LDA) ice phase. Reported inelastic mean free paths for vitreous water at 200keV are not as prevalent as at 120keV[129–132]. Reported value at 120keV range from 85-274nm and 302-392nm at 200keV. Equation 2.32 calculates an optimal LDA ice thickness of 600-800nm at 200keV. TEM work has been done on significantly thicker specimens[133,134]. Assuming the specimen fabrication procedure discussed later in this chapter produces an ice layer as thick as the manufacture reported specimen thickness of 30nm, the optimal thickness of LDA ice predicted by 2.32 is at least an order of magnitude larger.

Choosing specimen thickness solely based on 2.32 neglects other downsides from the electrons interacting with an increased volume of material such as decoherence. The SNR increases at larger specimen thickness due to increasing phase shift, but at the loss of contrast and coherence. At the optimal thickness, contrast decays by C_{inel} in equation 2.13. In a similar vein to specimen thickness, the material composition of the specimen affects the phase regime, weak or strong, the optimal thickness, and stability while under degradation. Biological specimens are especially susceptible to degradation resulting in 'ideal' low dose imaging setups[135–138], and degradation can increase in thicker specimens.

A brief example to conclude the above barrage of equations. Using equation 2.5, if the desired voltage resolution is 0.1V and the thickness of LDA ice is 30nm, the required phase sensitivity is 22mrad. If the ice thickness is at the upper range from equation 2.32, 600nm, the required phase sensitivity is only 437mrad. Assuming SNR = 3 and the number of electrons per reconstructed pixel is 1E4, the required contrast to achieve 22 and 437mrad is 0.64 and 0.032 respectively. This demonstrates the potential value of using thicker specimens.

2.1.5 Modifications to Increase Sensitivity

For the JEOL 2100F, there is a large magnification separation between Holo-L and Holo-M, 6,000 vs 100,000 respectively that results in a significant difference in the FOV as seen in Table 2.1. There are both advantages and drawbacks to each of these holography modes depending on the type of specimen and the desired information. Near atomic resolution off-axis electron holography was achieved in the mid 80s[139] with more-recent angstrom resolution[140,141] achieved due to C_S correction and direct detection cameras. At lower magnification and

resolution, studies of doped semiconductors[142,143] and magnetic particles[83,144] have also been done.

Modification to the effective magnification in each of these modes can be achieved through individual adjustment of each lens' power by use of the Free Lens Control (FLC) panel. The adjustment with FLC is intended to modify the predetermined lens configurations to achieve different magnifications, focus conditions, and resolutions than are accessible in Holography mode as listed in Table 2.1. This FLC modification was attempted to decrease the fringe spacing and increase contrast in Holo-L mode resulting in an increase of the magnification. A factor of two improvement in fringe spacing to 3nm was made while the contrast remained roughly constant at 10%. Unfortunately, the use of FLC to reduce fringe spacing below 3nm resulted in a loss of coherence that could not be immediately overcome for the specimen geometry used.

There are a total of 10 lenses controlled through the FLC panel as shown in Figure 2.2. Unfortunately, adjustment of just one lens is seldom sufficient or practical because many of the lenses are coupled in their effect on the resulting image. In Holography mode, IL1 is completely turned off because the biprism is located at the center of this lens. As a general rule, lenses above the specimen change the illumination condition: brightness, diameter, and convergence angle. Lenses between the specimen and biprism simultaneously change the focus at the biprism and the magnification at the biprism. A higher magnification at the biprism results in a smaller field of view but a higher magnification of the specimen.

Figure 2.2

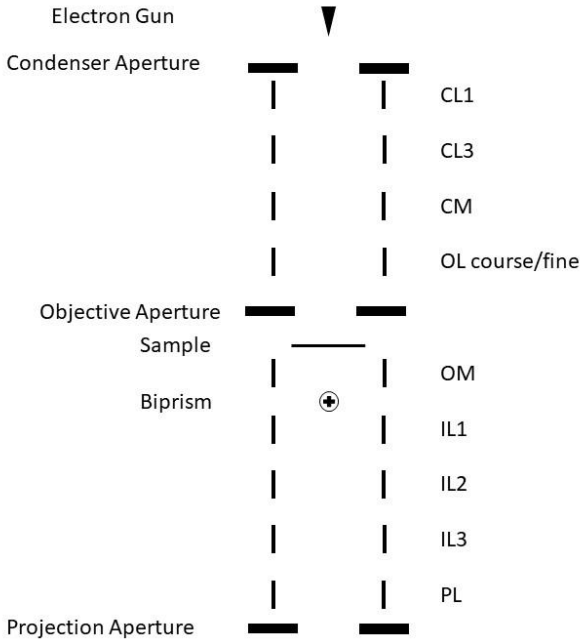

Figure 2.2: A schematic of the lens order and shorthand naming convention in the JEOL 2100F.

Lenses below the biprism increase magnification. When adjusting lens power individually, start with a top-down approach above the biprism and a bottom-up approach below. As always, a cyclic process is needed to ensure adjustments in one lens are retained as other lenses are further adjusted. Typically, adjusting the lenses above the specimen first is easier than the lenses below the specimen. The selective area (SA) aperture is located nearly coplanar to the biprism, so the SA aperture is never used when the biprism is inserted into the column to avoid possible collisions.

2.2 Limitations of Holography

Off-axis electron holography enables access to the ever-elusive electron phase. With that phase knowledge, the projection of the 3D electric and magnetic fields into the 2D image plane can be mapped within the limits of phase detection (and the other EM caveats). The advent of

field emission guns, C_S correction, direct detection cameras, and ever-improving specimen stability and drift correction provides holography a surprisingly strong platform to investigate a wide variety of systems where the additional knowledge of the electric and magnetic fields of the system could improve their fabrication, understanding, and modifications. However, holography is also paired with some rather challenging obstacles that sometimes cannot be overcome.

The primary issue is geometry. Whether that is specimen thickness or fabricating a vacuum path for the electron beam close enough to a desired feature, the geometry challenge can often be overcome, but not always. Difference holography can be used, but only in limited cases where the phase and material characteristics are well known. Sometimes a hole can be drilled with a focused ion beam, or a section can be removed. None of these options work every time though. Thickness is the other geometric challenge. Some systems such as cryo-EM necessitate "thin" specimens under 100nm while other systems such as semiconductors may require chemical or mechanical thinning after fabrication to achieve proper transmittance. Fabricating a cryogenic specimen that is >100nm thick could drastically affect the quality of the vitreous ice and the stability under the beam. For holography, cryo-EM falls victim to insufficiently thick specimens resulting in insufficient phase shift and SNR whereas semiconductor systems can be too thick resulting in decreased transmitted intensity and radiation damage. Thickness uniformity is also a challenge. Thickness variation on the scale of the feature size will result in inaccurate phase maps because neighboring electrons will have passed through differing amounts of material and will not remain coherent thus behaving differently in the post-specimen optics.

Specimen conductivity is challenging to address, especially in semiconductor systems where excess charge build up from the incident electrons can produce electrostatic bias and

additional phase shift. Electron source challenges couple with the specimen geometry challenges. Insufficient coherence reduces fringe density and brightness reduces the minimum detectable phase value. Brightness and coherence couple with drift. High quality cameras and inventive grid design can substantially reduce the effect of drift[145], but these are difficult to engineer. Not every TEM has a sufficiently high-speed camera and not every specimen support can implement a design to reduce drift. The Gatan Orius SC 1000A camera used in this work is not ideal for holography because the detector gain curve is nonlinear, and it exhibits pixel readout correlations. Nevertheless, modern TEM advancements have substantially advanced the capabilities of off-axis electron holography.

2.3 Cryogenic Specimen Fabrication

The predominant guidance in the field of cryo-EM for specimen fabrication is thin amorphous ice. Ice thickness is predominantly linked to grid thickness, blotting time, and solution-grid chemistry. Reducing the multiple scattering contribution in the transmitted beam from ice surrounding the object of interest –most commonly a biological molecule, protein, or virus in cryo-EM[146]—is a primary goal for thin ice. Other considerations such as solubility modifications that affect specimen fabrication are relevant to the field of cryo-EM[56,147,148] but will not be discussed here, since they mostly do not pertain to the solutions used in this work.

2.3.1 Grid Selection

Most cryo-EM work is done on Quantifoil grids (Quantifoil Micro Tools GmbH). Quantifoil consists of a 3mm diameter metallic mesh TEM grid supporting a thin a-C film. The a-C thickness was confirmed at 30nm with a scanning electron microscope using a batch of

Quantifoil grids from Ted Pella. The film is typically patterned with a variety of different circular hole sizes and spacings but can also be purchased with elliptical and square holes. Circular hole diameter ranges from 0.6-17μm and spacing between 1-100μm. The larger diameter and spacing options are far less common with the three most common hole diameters being 0.6, 1.2, and 2μm, in order of decreasing predominance. The grid mesh composition is Cu, Au, or Ni with mesh pitch offerings of 200, 300, or 400 (1"/mesh pitch). The film can be standard a-C, ultrathin a-C, SiO_2, or UltrAuFoil where the entire grid and film are both made from Au with a membrane thickness of 50nm. The benefits of UltrAuFoil mainly center around thermal stability and drift[149,150]. Further improved cryo-EM specific grids have been made to improve drift and membrane buckling by implementing a hexagonal membrane hole[145]. The second grid type used was holey carbon (SPI 3630C, Structure Probe Inc.). With similar thickness and mesh options, the main drawback to holey carbon is the random distribution of hole size and spacing.

2.3.2 Specimen Solution

Within cryo-EM specimen fabrication, the most challenging component is suspending the solute particles in an effective manner that allows for minimal disruption when blotted. The data presented utilizes two different specimen solutions: pure deionized (DI) water and charged Au nanoparticles suspended in DI water. The pure DI water specimens were used to understand the base system. Nanoparticle solution used for data collection was a 2:1 ratio of DI:nanoparticle solution resulting in a concentration of 1.067nM (1E14 particles/mL).

The addition of 30nm Au nanocubes by NanoPartz (B1C-30-3MPA-DIH-1.25-0.5) shown in Figure 2.3 had the purpose of enabling measurement of electric field and its effects on

the surround solution. The nanocubes were functionalized with 3-Mercaptopropionic (3-MPA) acid, an organosulfur compound that is bifunctional with both carboxylic acid and thiol group[151–154]. 3-MPA was chosen over longer (5- or 7-) MPA because the carboxyl density, uniformity, and chain stability are better at the shorter 3 carbon chain length. The functionalization results in a surface charge density of 3 e^-/nm^2 meaning a nominally sized and shaped nanocube has a total surface charge of 2.59E-15 C. Observationally, nanoparticles tend to distribute more uniformly on holey carbon films than on Quantifoil films. An exact reason was not determined for this observed behavior but could be related to charge that terminates the carbon at the edges of the Quantifoil holes.

Figure 2.3

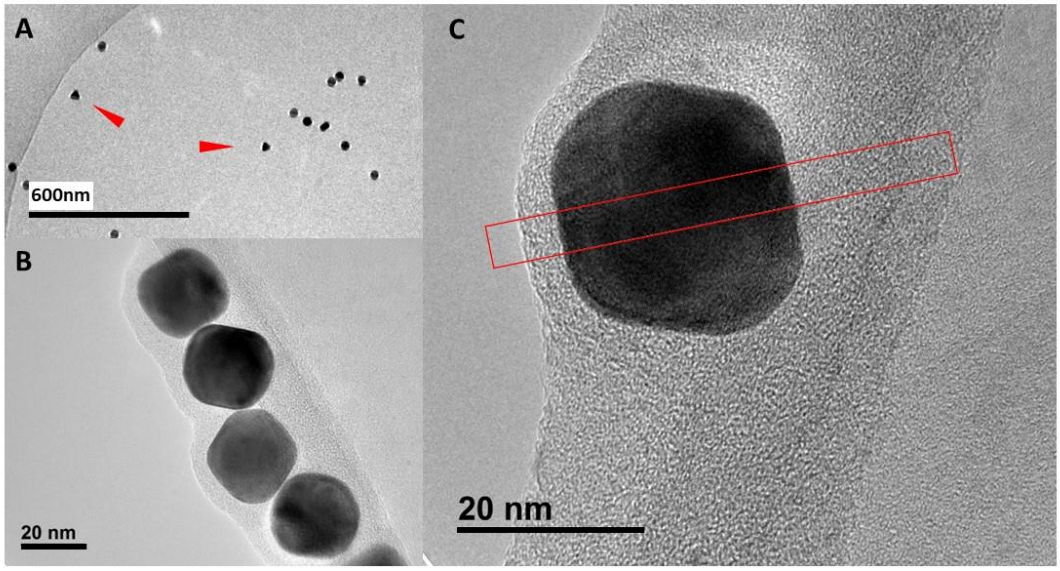

Figure 2.3: Mass contrast electron micrographs of functionalized Au nanocubes. In (A), nanoparticles appear triangular at the red arrows while other nanoparticles are more sphere-like. However, the lower magnification could account for this appearance. In (B,C) nanoparticles appear cube-like with expected corner curvature. The diameter of the cube in (C) was measured using Digital Micrograph with the red box indicating the region measured which gives a 25nm width.

The complexity normally found in biological cryogenic specimen fabrication[148,155,156] was significantly mitigated by using charged nanoparticles in DI water. Although particle migration to the air-water interface is a concern, specifically investigating the particle's z location in the ice was not done because interaction with the interface would not degrade the quality of the nanoparticle. The thickness of the ice was estimated to be nearly identical to the 30nm thick Quantifoil a-C film by using mass-thickness contrast TEM across the diameter of representative LDA-filled holes. The Au nanoparticles were not all cube shaped, as indicated in Figure 2.3A by the two red arrows, which appear more octahedral. Also, the diameter of the nanoparticles was not routinely 30nm as seen in Figure 2.3C where the diameter was measured in Digital Micrograph at 25nm. Both variations are attributed to the growth process. The surface energy of the {111} is lowest of all Au facets, so Au will preferentially grow along the {111} resulting in a preference for octahedral shape. The next lowest energy facet is {100} which results in a cube. A balanced combination of {111} and {100} results in a cuboctahedron[157]. Regardless of the actual dimension and geometric shape, the flat edges of the nanoparticles could enhance the signal from a tightly bonded layer of ions from the solution, for example a Stern layer[158–162]. This consequence will be discussed in chapter 4.

2.3.3 Cryogenic Plunge Process and Specimen Transfer

Preparing the cryogenic specimen is a three-stage process: solution-grid preparation, solution-grid plunge, and specimen transfer. The previous two sections have gone over the type of grids used and the solutions used. The plunge process is straightforward both in principle and practice, though it can be challenging to implement. The last remaining fabrication challenges

are determining an ideal blot time to yield an ideal thickness and transferring the plunged grid into the TEM holder.

There are three commonly used cryogenic plunge freeze systems, besides custom made ones: Gatan CP3, Leica EM GP2, and Thermo Fisher Vitrobot. The Gatan CP3 is by far the least technologically advanced of the three, lacking climate control inside the blotting chamber, forced plunge actuation, and blotting force control. The Leica and Thermo Fisher systems have all three features which is why the Vitrobot and EM GP2 are the first and second most used respectively. A Gatan CP3 and Thermo Fisher Vitrobot were used to prepare the specimens reported on in chapter 4.

Before loading a grid into the plunge system, grids are made hydrophilic using a weak plasma, commonly a PELCO easiGlow. Fresh grids from the distributor are hydrophobic, which is problematic if the solution is water-based. Special cryo-tweezers hold a treated grid in the plunge system. A few μL volume of water is pipetted onto the grid. Excess solution is blotted away, and the plunge arm rapidly moves the tweezer tip and grid into the waiting liquid ethane. The removal of excess liquid reduces the total heat capacity facilitating rapid cooling to achieve a vitreous ice[155]. Liquid ethane is used as the cryogen because of its superior cooling ability over contenders such as propane and slush nitrogen[155,163–165]. With the specimen at liquid nitrogen (LN) temperatures, the specimen is carefully transferred to a similarly cooled storage puck that holds four total grids.

After the specimens are made, either storage or imaging takes place next. If the specimens are intended for storage, the grid storage puck is placed in a larger storage puck and placed in a LN dewar. When imaging is planned in a non-cryo dedicated TEM, the side-entry

cryo-holder is cooled in the transfer stage and the grid storage puck is inserted into an adjacent recessed area while submerged in LN. When the holder has reached LN temperature, the tweezer tips are cooled in the LN, the grid is grasped by the tweezers, and the grid is inserted into the holder blade. Cooling the tweezer tips reduces specimen heating and possible alteration of the vitreous ice state. It is recommended by Gatan to keep the specimen submerged in LN the entire time while being transferred into the holder. Following these steps helps prevent the specimen from warming during transfer. The main drawback of transferring a grid while submerged in LN is the grid can be dislodged from the correct location in the holder and either float away or require recentering the grid in the holder by the movement of LN.

An alternate method is to keep the grid storage puck submerged but let the LN boil away from the holder. This is possible because the transfer stage is at roughly 45° angle, so the holder blade is vertically higher than the grid storage puck. The method does prevent the grid from floating away after releasing the tweezers, but there is a risk the specimen could warm or form ice crystal condensation. Considering the LN is evaporating just above the liquid layer, there is a significantly reduced chance of water vapor condensation. Specimen warming is the concern if transferring under nitrogen vapor. However, since LDA crystalizes at 115-160K[166–169], as long as the specimen is kept nearly submerged the likelihood of crystalizing within one second is minimal in LN vapor.

Specimens used in chapter 4 were made as follows. Quantifoil 300 mesh R2/1 (Ted Pella Inc 667-CU, 2μm hole diameter and 1μm spacing) and R2/2 (Ted Pella Inc 657-CU, 2μm hole diameter and 2μm spacing) a-C Quantifoil TEM grids were made hydrophilic using PELCO easiGlow (Ted Pella Inc) at 0.4mbar for 25 seconds with a positive current of 10 and 20mA for

R2/1 and R2/2- respectively. Grids were loaded one at a time into a Gatan CP3 cryo-plunge system (R2/2) or Thermo Fisher Vitrobot (R2/1) where 3μL of solution was placed onto the treated grid, blotted for 5s (R2/2) or 4s (R2/1) with filter paper (VWR 28309-967 or EMS 71166-65) and plunged into liquid ethane. The grid was loaded into a Gatan 914 High Tilt Cryo holder (#07118081) and inserted into a JEOL 2100F Schottky field emission gun operated at 200kV at -176C and -179C respectively. Electron holography was performed with a JEOL EM-20171 electron biprism. A Gatan Orius SC 1000A camera acquired the images.

Chapter 3: Electron Hologram Analysis and Model Development

A suitable hologram ready for analysis is acquired following the procedures described in chapter 2. The raw images are first analyzed to extract phase maps, identify regions of interest, and perform statistical analysis, outlined in section 3.1. Then electromagnetic models are developed, compared with experimental data, and refined to improve agreement, described in section 3.2.

The choice of analysis software generally falls to three possible options: Digital Micrograph (DM), MATLAB, or Python. Digital Micrograph is often chosen because of the HoloWorks software package and integration with data collection. MATLAB and Python allow for more control over the exact process and data handling but come with a drawback in that often the user must generate the code themselves. MATLAB was chosen for hologram and simulation analysis because of a greater familiarity with the language and interface. As well, implementations of different unwrapping algorithms from published research are readily available. Electromagnetic modeling benefits from partial-differential equation numerical software. For this function, COMSOL was chosen for its ease of use, extensibility, and mesh quality.

3.1 Electron Holography Analysis

The hologram seen in the TEM is captured on a CCD camera and saved as a dm3 file in DM software. The dm3 file is imported into MATLAB using a readily accessible dm3 import script[170] and a four-step process to extract the phase data follows: (1) Fourier transform of the hologram image, (2) centering sideband selection and mask, (3) inverse Fourier transform, and

(4) phase map calculation. These steps are described in section 3.1.1 below. The trigonometric relationship in the phase map calculation step involves a branch cut in the complex plane and extending the phase map to unwrap the branch cuts is beneficial when comparing to models. This unwrapping process is discussed in section 3.1.2. The final section, 3.1.3, addresses an ambiguity from step (2) above, where slight shifts add a linear slope (i.e. plane wave) to the phase map. Section 3.1.3 describes how to remove this slope when comparing to the model.

3.1.1 Phase Extraction

An electron hologram of vitreous DI water on a Quantifoil grid is shown in Figure 3.1A. Three roughly horizontal rows of 2μm diameter holes are visible. The top and bottom rows are determined empty and filled, respectively, based on their contrast to the surrounding carbon film. The central row of holes in Figure 3.1A displays the electron hologram that result from an applied voltage to the biprism and the overlap of a neighboring row of holes. There is a random distribution of darker, non-vitreous ice particles throughout the image indicated by green triangles that are attributed to ice nanoparticle accumulation from vapor when the specimen is transferred from LN2 to the cryo-holder. Figure 3.1B is the result of adjusting the electron optics and increasing the biprism voltage of the outlined region in Figure 3.1A. The slight mismatch in relative contrast range exhibiting a vertical line dividing the two holes is attributed to the stitching algorithm of the camera that combines the two discrete CCD detectors together into a single image. This slight offset is not observed in the extracted phase shown in Figure 3.1D and therefore is not considered further in the analysis.

Figure 3.1

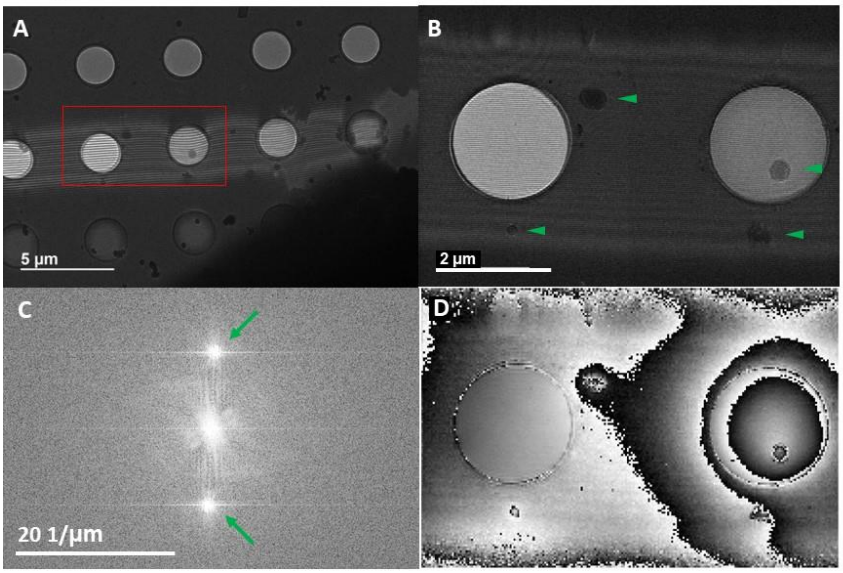

Figure 3.1: An electron hologram image of vitreous DI water on a Quantifoil grid (A) where a red box indicates a region of interest shown in (B). A Fourier transform of (B) results in (C) showing a central peak and 2 sideband peaks. The phase map (D) of (B) displays regions of constant phase (left hole) and changing phase (right hole). Branch cuts in the MATLAB atan() function appear as contour lines in (D) with the change in color from white to black. (B,D) share the same scale.

To access the phase information contained in Figure 3.1B, a Fourier transform of B is taken resulting in Figure 3.1C. Recall equation 2.11, the Fourier transform is

$$\mathcal{F}\big(I_{hol}(\boldsymbol{r})\big) = \delta(\boldsymbol{q}) + \mathcal{F}\{A_i^2(\boldsymbol{r})\} + \quad \text{centerband}$$

$$\delta(\boldsymbol{q}+\boldsymbol{q_c}) \otimes \mathcal{F}\big\{A_i(\boldsymbol{r})exp\big(i\phi_i(\boldsymbol{r})\big)\big\} + \quad \text{sideband +1}$$

$$\delta(\boldsymbol{q}-\boldsymbol{q}_c) \otimes \mathcal{F}\big\{A_i(\boldsymbol{r})exp\big(-i\phi_i(\boldsymbol{r})\big)\big\} \quad \text{sideband -1} \qquad (3.1)$$

where terms for a peak at the reciprocal space origin from the reference wave, a peak at the origin from the bright field TEM image of the specimen, and complex conjugate peaks at $\mathbf{q}=\pm\mathbf{q}_c$ for the image wave function[123] are present. All four terms manifest in Figure 3.1C, but most importantly, the sideband peaks located at $\mathbf{q}=\pm\mathbf{q}_c$ form the basis for phase map extraction. Note

these terms alone carry the phase information which is lost in the first two terms and during typical TEM image acquisition.

The central intensity peak is flanked by two symmetrically located sideband peaks that contain the phase information necessary to determine the electric and magnetic behavior of the specimen. These sideband peaks correspond to the fundamental cosine frequency of the interference fringes where their separation from the central peak primarily depends on the applied biprism voltage[171]. Either sideband is selected by masking, because they are complex conjugates of one another, and the location of maximum intensity for the sideband is centered by rigid shift onto the central intensity peak. The optimum mask radius depends on the exact specimen composition in general[172], and for a strongly scattering object, the optimal radius of the mask is 1/3 the carrier frequency[104]. An inverse Fourier transform is then performed on this new, modified frequency-domain image resulting in real and imaginary components, $\mathfrak{I}$ and $\mathfrak{R}$, for the complex image. The amplitude and phase images are calculated using

$$A = \sqrt{\mathfrak{I}^2 + \mathfrak{R}^2} \tag{3.2}$$

$$\phi = \arctan\left(\mathfrak{I}/\mathfrak{R}\right) \tag{3.3}$$

Applying equation 3.3 results in Figure 3.1D, the wrapped phase image of Figure 3.1B. The phase map from 3.3 is directly related to the electric potential and magnetic field of the specimen by equation 2.4.

Before phase unwrapping is performed, two immediate observations can be made of Figure 3.1D. First, the steps in phase occurring at the transition from light-to-dark regions are separated by 2π because arctan is bounded and exhibits a branch cut in the complex plane. Second, regions of identical overlapping materials have zero phase shift, as expected, as

observed in the left hole in Figure 3.1D. The reduced pixel density of Figure 3.1D relative to 3.1B originates from the fringe spacing of the original hologram and the inverse Fourier transform process. The fringe spacing of the hologram limits the spatial resolution of the technique. Finally, the frequency spread at the sidebands in Figure 3.1C results from local phase shifts caused by the specimen.

3.1.2 Phase Unwrapping

To aid in matching experimental phase maps to a model, the phase maps were unwrapped into an unbounded phase range. The choice of unwrapping the phase map is only one of many methods used to analyze the phase information. Other methods to display and interpret the phase data include[104]: (1) as a raw, unwrapped phase map with 2π jumps, (2) as an unwrapped phase map, (3) as an interferogram where a phase ramp is added, (4) as the interference image where cos(φ) is plotted, (5) as the phase amplified image where cos(nφ) is plotted for small integers n giving more frequent branch cuts, and (6) as the differentiated image highlighting 2π jumps. Phase data option 2 was selected from the above list because comparison to an electromagnetic model is more straightforward.

The use of equation 3.3 results in a wrapped phase image that has a saw-tooth shape because the arctangent function is bounded in the range (-π, π]. To obtain a continuous phase map, the 2π phase jumps must be stitched together by a phase unwrapping algorithm. A simple view of the unwrapped phase is given by

$$\phi(x_i, y_j) = \varphi_{i,j} + 2\pi k_{i,j} \tag{3.4}$$

where ϕ is the unwrapped phase, φ is the wrapped phase, and k is an integer that stitches neighboring pixels together. Unfortunately, phase unwrapping propagates any initial errors

throughout the entire image. To understand this, consider the following example. A wrapped phase image is unwrapped pixel-by-pixel. If any one neighboring pair of pixels is incorrectly unwrapped due to noise or a false wrap in the phase, both pixels will be incorrectly unwrapped, thus propagating throughout the entire phase image[173]. A least squares transport of intensity equation (TIE) phase unwrapping algorithm [173](PUA) was used in this dissertation for all phase unwrapping but other algorithms can be applied for various purposes[174,175].

As mentioned, the arctangent function is used to calculate the phase image from $\mathfrak{I}$ and $\mathfrak{R}$ of the complex image. An ideal branch cut location for the phase map is selected by comparison from a 15° rotation of the phase data through (0, 2π] and plotted in Figure 3.2 at 30° intervals. The 2π phase jump moves as shown in the top row of Figure 3.2 from 0° through 90° and continues to 330°. A branch cut rotation is selected from the possible rotations so that no phase jump occurs in a boundary of any region of interest and the unwrapped image contains no regions of incorrectly unwrapped phase that is, regions that are shifted by 2π. Careful selection of the rotation is not always necessary but is done to intentionally limit the extent of unwrapping errors. In the case of Figure 3.2, 0° rotation was chosen because no phase jump occurs in the left hole, the phase jumps at the right hole are sufficiently separated from the hole perimeter, there is a minimum appearance of noise when compared to the 330° rotation, and the unwrapped phase has the fewest number of incorrectly unwrapped pixels. Figure 3.1D and Figure 3.2 0° are the same.

Figure 3.2

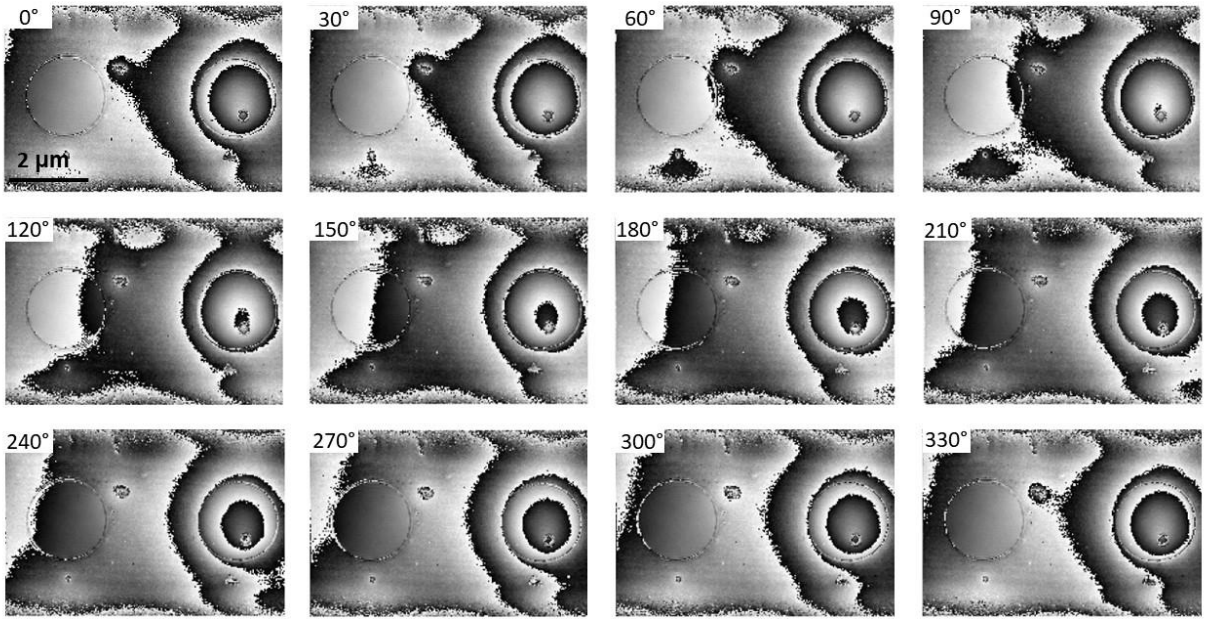

Figure 3.2: A tableau of wrapped phase images where the location of the branch cut is varied from 0° to 330°. The scale bar in 0° is shared among all images.

The rotated phase map in Figure 3.3A is unwrapped using the least squares TIE PUA[173] resulting in Figure 3.3B. The PUA leaves no apparent residual from the 2π phase shifts at the right hole. With an unwrapped phase map such as in Figure 3.3B, a variety of comparisons and further analysis can be done. Mean inner potential calculation[74–76], charging and doping[83,144], magnetic field reconstruction[176–179], electric field reconstruction[180], and more can be investigated depending on the system under study by using equation 2.4.

Figure 3.3

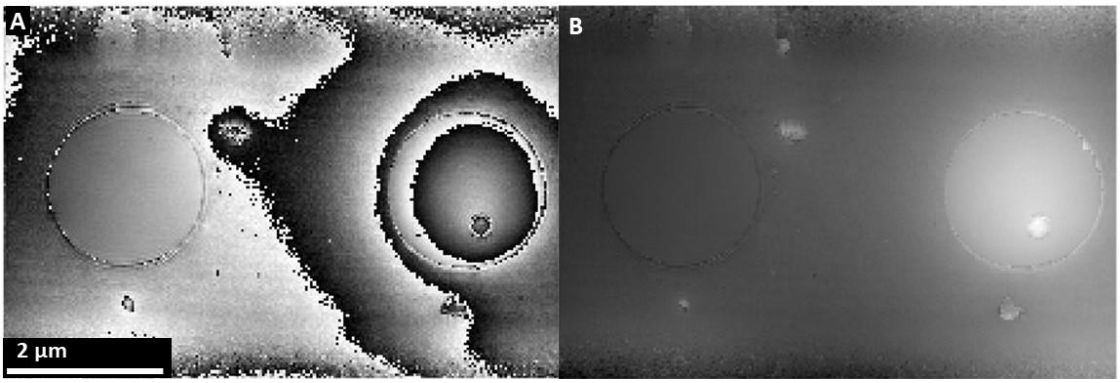

Figure 3.3: Wrapped phase from Figure 3.1D with zero branch cut rotation (A). The unwrapped phase image (B) of (A). (A,B) share the same scale.

It should be noted at this point that common guidance strongly recommends taking a reference hologram of vacuum space to eliminate distortions from the biprism itself and between the biprism and electron detector[117]. However, the method of reference phase subtraction does not always correct phase distortions[128]. For this reason and geometric limitation of the specimen, the analysis in chapter 4 does not include a reference phase subtraction and the interpretation should be informed, but not limited, by the lack of a reference hologram.

3.1.3 Plane Subtraction

The extracted phase map for the Quantifoil specimens does not always have a peak at the center of each hole. This can be in part from lack of a reference phase map, not exactly selecting the sideband center, and an insufficient mask of the sideband. To account for this non-centered peak, a plane fit and subtraction is performed as follows. The center pixel of the Quantifoil hole is identified and the distance between the center and every pixel in the phase map is calculated. The radius of the hole is calculated from the center and a threshold is implemented on the distance values. This is achieved by keeping all pixels that are one pixel smaller than the hole

radius. Further subtracting some number of pixels from the actual radius typically increases the accuracy of the following fit by eliminating hole-edge pixels that may have unwrapping errors or other artifacts. This justification will become clearer in chapter 4.

A 2D parabolic fit of the pixels within the hole is performed. Then a linear plane is subtracted from the data so that the center of the hole and extremum are coincident. A constant offset of the phase map does not alter any structure or feature contained within and can be applied to the phase map because holography measures the relative phase difference. A linear plane offset can also be applied to the phase map because this shift is mathematically equivalent to shifting the arbitrarily selected sideband center location in Fourier space. The combination of a constant offset and linear plane adjustments changes values of the phase map but does not affect the analysis in chapter 4. The result of the plane subtraction is shown in Figure 3.4 where contour plots were chosen to better illustrate the movement of the phase peak location with the plane subtraction. The specimen, hologram, and unwrapped phase map used in Figure 3.4 are not the same as in Figure 3.3.

Figure 3.4

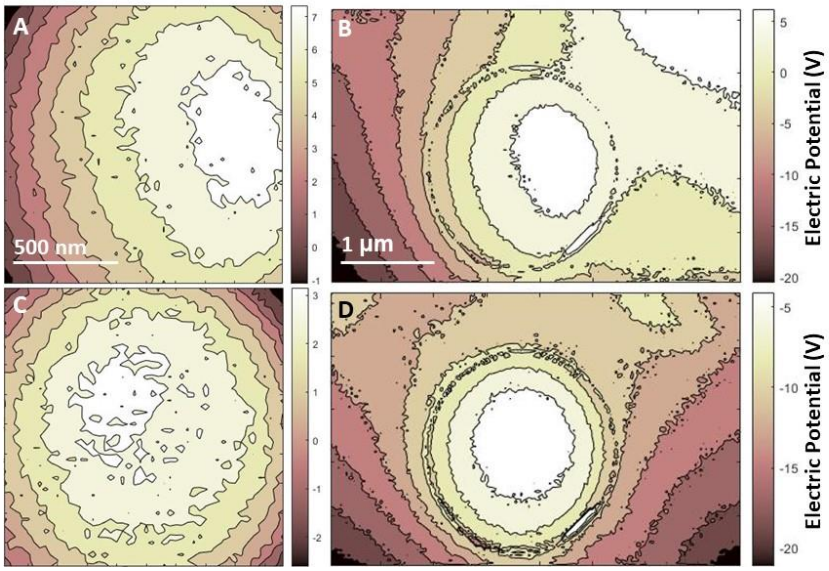

Figure 3.4: Contour plots (A,C) display the central square region of the hole in (B,D), respectively. (A,B) contour plots display the electric potential profile before a linear plane subtraction and (C,D) display the same data after the plane subtraction illustrating the shift of the peak potential value to the center of the hole. The scalebars in (A,B) apply to (C,D) respectively.

3.2 Simulation

Comparison of the hologram phase data to theoretical values and a model system aids understanding of the observed phenomena and can validate more recent descriptions of the physics. To this end, a model geometry was built in COMSOL because it incorporates well-established physical relationships and material properties into an interface that is straightforward to implement.

3.2.1 Goal of the Model

Simulations of the specimen were done in COMSOL to generate comparative data for analysis in conjunction with the experimentally acquired holography data. Detailed control of the geometry and physics allows for parameter extraction that would otherwise be nearly

unattainable such as LDA ice surface or volume charge densities, electric field and potential, and material influence on those same parameters. COMSOL was chosen because of its robust meshing system and relative ease of use. Two simulations were done focusing on related physics but with different intentions. Firstly, a 3D model attempts to quantify the extent of specimen charging that occurs on the LDA ice. A model geometry was built, and electrostatics implemented with a variety of physically possible conditions. The second model was built in a 2D axisymmetric environment and simulates the ionic distribution from a charged nanoparticle before the plunge process vitrifies the water.

3.2.2 3D Electrostatic Model of Water

The first model, and possibly the simpler to construct, is the electrostatic model where only charged planes, ground planes, and charge conservation are included. Figure 3.5A defines the geometry implemented and Figure 3.5B is a zoomed in, not to scale, vertical slice through the center where the a-C grid and hole are the faint black lines. The goal of this simulation is to look at and understand the electric potential of a 2μm diameter hole in a Quantifoil grid filled with DI water that has been vitrified through the plunge process detailed in chapter 2. Electrochemical effects are treated in the next section. Throughout this section, the primary parameter is the charge in or on the LDA ice. Considerations of ground plane location and ice thickness are addressed in chapter 4.

Figure 3.5

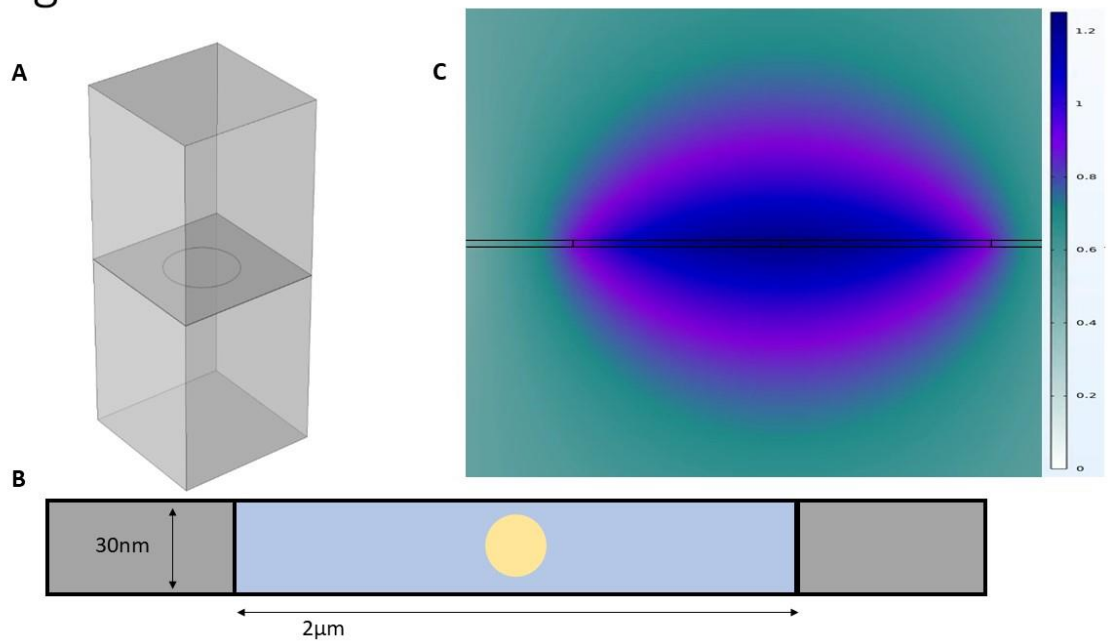

Figure 3.5: Geometry implemented in electrostatic COMSOL simulation (A) where a 4x4x8μm vacuum box surrounds a 30nm thick a-C film with a 2μm filled hole of DI water. A cross section, not to scale, through the a-C film (B) shown in gray surrounding the blue vitrified water containing a gold nanoparticle roughly 20nm in diameter. (C) A slice in the z direction of the electric potential field result showing 2 μm above and below the a-C film.

A representative geometry consisting of a 30nm thick a-C sheet with a 2μm diameter and uniform water thickness filled hole surrounded by a 4x4x8μm vacuum box was implemented. The vacuum volumes create an interface with the a-C and do not overlap. The vacuum volumes are required because holography is sensitive to the entire electric potential each electron passes through from emission to detection and COMSOL does not calculate said potential outside the defined geometry. A single hole was simulated, and confirmed to be sufficient, because the electric potential within a 4x4μm region drops off fast enough that a nearest neighbor contribution would not change any analysis or conclusions in chapter 4. The perimeter of the a-C sheet was always held at ground. The simulation data were exported to MATLAB and summation of the resulting 3D phase matrix was done in the z direction. This z-direction

summation is the numerical equivalent of the integration from equation 2.5. The mean inner potential for water and a-C of 3.5V[72,76,181] and 9V[182] respectively is discussed in chapter 4.

Surface charging of the LDA ice and a-C is assumed because their resistivity at LN temperatures is on the order of $10^{9}\Omega$cm and $10^{-2}\Omega$cm respectively[149,183–187]. Surface charging, sometimes called the Berriman effect[188,189], is assumed over a volume charging model because secondary electron emission at the surface is the primary mechanism for charge generation[190]. Incident electrons cause material electrons to escape the ice and either recombine with the ice at some other location, absorb onto the a-C, or escape to the vacuum of the model, which represents absorption by a ground plane somewhere in the TEM. A value of 1E-5C/m^2 was applied to the electrostatic simulation unless otherwise stated.

Two further geometries are discussed in chapter 4 using the above-described electrostatic model.

3.2.3 2D Poisson-Boltzmann Model of Ionic Distribution

The above 3D model ignores the ion distribution if a charged particle were added to the solution. A second simulation is constructed to predict the ionic distribution of H^+/OH^- in the presence of a charged nanoparticle but absence of any added salt. This reflects the surface-acid-modified particles introduced in chapter 2. The geometry is similar to that used in the 3D model but in a 2D axisymmetric coordinate system chosen for computational speed. Choosing the axis of rotation to be the direct middle of the nanoparticle in Figure 3.5B and adding a vacuum space above and below the 30nm thick water-carbon sheet creates the 2D model. Ground was set at the outside edge of the carbon, farthest from the rotation axis. The same COMSOL electrostatics node from the 3D model was used, but the Poisson-Boltzmann (PB) equation was chosen to

govern the ions[191,192]. The classical PB theory assumes a dilute solution of point charges with mean-field electrostatics when considering electrolytes.

An alternate approach would be to use the built-in Transport of Dilute Species (tds) node which obeys the Nernst-Planck equations but does not have the same zero flux constraint as PB or to use a time-dependent solver instead of steady-state. Both alternate approaches were avoided because the PB method, corrected for steric effects, predicts the correct ionic distribution to a reasonable extent at lower computational cost and reduced complexity. Also, the tds model requires additional assumptions that are not easy to justify. Since the intention of the model is to provide a reasonable estimate of the ionic distribution, not an exact calculation, the PB theory used is a reasonable heuristic model.

The primary benefit in applying PB is the increased simplicity of the model, and it works well for dilute electrolytes, in which aqueous H^+/OH^- are typically considered. The math, justifications, and assumptions are laid out in detail in section 2B and specifically equation 25 in reference 191. The addition of a packing factor, set to 1E-3, prevents an exponential increase in proton concentration near the nanoparticle surface. Additionally, the proton concentration can change the equilibrium condition for a fixed charge impacting the effective surface charge at the nanoparticle boundary[193].

The primary assumptions in this model are the following[191,192]: the reservoir is sufficiently large, the functional form of the solution free energy follows equation 24 from reference 191, microscopic details of the solvent and ions are ignored, the electrostatic potential and charge density are ‘smooth’, and ion-ion correlation effects are ignored.

The primary drawbacks to this model are the following: the reservoir (volume of water) at the boundary is insufficiently large to support the PB model; the charge density of the nanoparticle could be too high, resulting in an inaccurate description of the physics; the Boltzmann packing factor is an order of magnitude estimate; the air-water interface potential can span 10mV to > 3V[194,195] but is ignored; and the general lack of solution/interface complexity overlooks behaviors such as ion-ion interaction. The COMSOL tds model does not address all of these drawbacks.

These models all ignore the changes to concentrations and densities that might occur during plunge freezing and vitrification process. It is assumed that the cryo-EM process captures the room-temperature structure in a vitreous state. After the specimen is in the microscope, it may charge due to beam effects as described in the previous section. The Maxwell equations are linear, so numerical solutions from the two models can be combined by linear addition.

Chapter 4: Data Analysis and Interpretation

Now that the physics of holography, the specimen parameters, the methodology of data collection, and the methodology of simulation data creation have been laid out, analysis of the collected data is covered in this chapter. The simplest case, that provides the foundation for further complexities, starts with fully understanding the holograms that result from LDA ice of just DI water devoid of NPs. Identifying the phase shift and charging profiles, distortions, and comparison to the simulated data are the primary task. Investigation of more complex systems with charged NPs and weak electrolytes follows.

4.1 Beam Charging of LDA Ice

The most foundational experiment conducted, after initial testing to confirm electron holography and cryo-EM are compatible, was the investigation of charging effects from the electron beam on LDA ice. A hologram time series of LDA ice was collected using Quantifoil R2/1 grids fabricated using the process in chapter 2.

4.1.1 Time Series

Understanding the charging regime in which electron holograms are taken is particularly important[185,187,196–198]. The different physics between transient and steady-state specimen charging will impact the relative phase map from equation 2.5. Efforts have been made to understand the nature of specimen charging in cryo-EM using different techniques[185–187]. This charging could impact image quality in cryo-EM. Depending on the mechanism for charging and the sign of charge accumulation, setups can be developed that could improve or reduce resolution and sensitivity in cryo-EM. To that end, off-axis electron holography was used to investigate the time dependence of specimen charging.

A time series of consecutively acquired holograms was taken to determine which charging regime the specimens are in. Three time series were taken, but only two produced interpretable results. The third time series encountered biprism and lens instabilities that resulted in low quality holograms and is therefore ignored. Upon specimens equilibrating in the TEM, a low magnification (500X) scan for potential holography regions was conducted. The beam was blanked immediately upon identification of a possible holography geometry and the location was recorded. After the entire grid was scanned, a second, quick scan was done at each previously identified location at a 2kX magnification and an image was acquired as shown in Figure 4.1A, for reference, with a 1 second exposure.

A suitable geometry for R2/1 at 6kX requires at least one empty hole and one LDA filled hole at 2^{nd}-nearest-neighbor separation because the hologram is optimized at this magnification and separation. Choosing nearest neighbor or 3^{rd}-nearest neighbor results in holograms with too few fringes or insufficient fringe contrast, respectively. The biprism is inserted, aligned, and voltage applied approximately 200μm from any one desired image location. Because the a-C film is not guaranteed to be flat across the entirety of the grid due to distortion from specimen loading, a second, quick alignment is done at a nearest neighbor grid location, being careful not to fully spread the electron beam to reduce any possible charging on the region of interest. Finally, the beam is blanked, moved to the recorded location, allowed to settle from translation drift, quickly centered on the desired hole if necessary, and a 4 second exposure is taken resulting in Figure 4.1B, a representative hologram of the two time series. After the first hologram exposure of each series, the electron beam is not blanked, and subsequent holograms are continuously recorded at 2-minute intervals. Both time series consist of four holograms recorded 2 minutes apart.

Figure 4.1

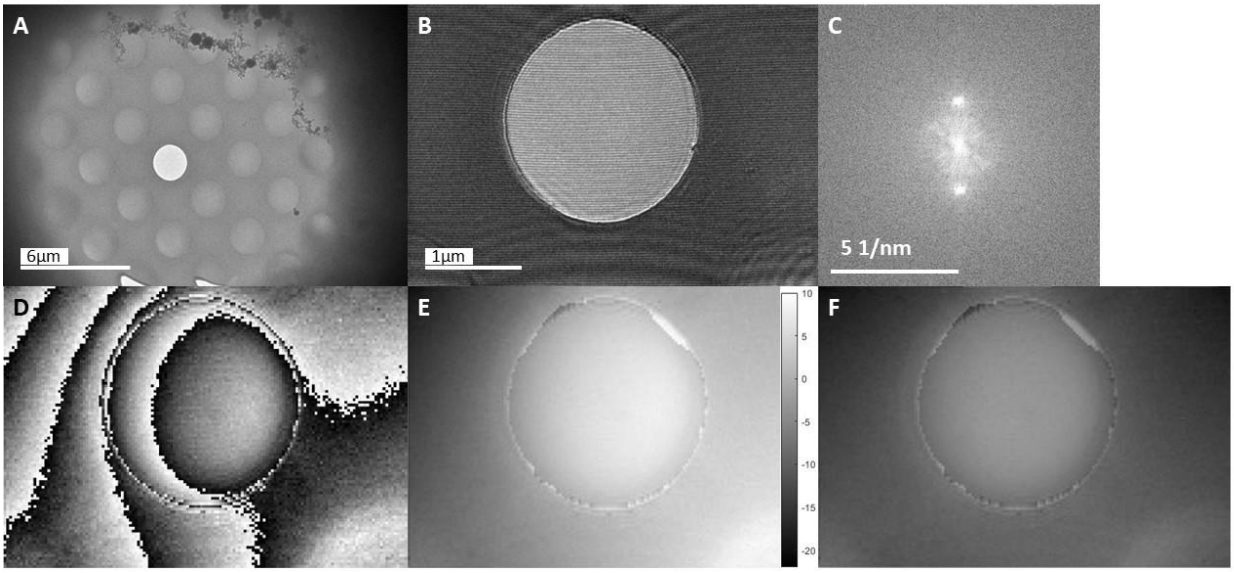

Figure 4.1: A 4 second exposure of the region of interest (A) for holography. The electron hologram (B) where the unfilled hole in (A) is overlapped with the 2nd-nearest neighbor directly below. The FFT (C) and unwrapped phase (D) with a $\pi/3$ rotation result in the unwrapped phase in (E). The plane subtracted (F) unwrapped phase map of (E). The scale bar for (D,E,F) are the same as in (B). (E,F) share the same color bar in radians.

With the time series record, the analysis described in Chapter 3 produces Figure 4.1 C-F. The top sideband was selected in Figure 4.1C and a $\pi/3$ rotation was applied to create Figure 4.1D. As discussed in chapter 3, phase unwrapping can have unexpected errors as shown at the top right of the hole in Figure 4.1E where the phase is unwrapped with a 2π phase shift compared to its surrounding. The effect of this unwrapping error will be discussed below. Recall the sole purpose of finding a suitable plane to subtract from Figure 4.1E is to center the phase peak in the hole of the specimen. The fact that the phase profile for the a-C is not perfectly flattened does not negatively impact the following analysis and therefore the asymmetry seen in Figure 4.1F between the top and bottom corners is irrelevant.

The most efficient way to analyze the phase profile of only the LDA ice is to select the phase data from the LDA ice region, omitting the phase data from the a-C region. This selection is done by using the same center finding and threshold method outlined in Chapter 3 to center the peak phase value:

identify the center of the hole, calculate each pixel's distance from the center, and threshold that distance by the radius of the hole. With the LDA ice data selected, an optimization algorithm was applied to scale simulation data to the experimental data.

As discussed in Chapter 3, finding an exact surface charge through iteration in COMSOL is not ideal and comparatively cumbersome. Therefore, a reasonable guess for the surface charge is used throughout most all the COMSOL simulations of 1E-5 C/m^2 and a search algorithm is implemented to find an appropriate scale factor for the surface charge. The built-in MATLAB function fminsearch uses the Nelder-Mead simplex algorithm which is described in detail here[199] and the corresponding documentation page at mathworks.com. The COMSOL data were exported with a 5μm vacuum box above and below the 4x4μm a-C sheet and a circle of radius 1μm with ground planes at the perimeter vertical surfaces of the a-C.

The nonlinear search algorithm is used in two steps. First, the scale factor and offset parameter between a COMSOL data set and the time series holograms is found and second, the 2σ (95% confidence interval) values for the scale factor are found. The first function to find the scale factor and offset, analogous to Chi-squared**,** is a sum of the squared differences between the hologram and COMSOL phase data. In the second application of fminsearch, the offset is held constant at the value found in the initial search. The second function, to find the 95% confidence interval values, searches for the upper/lower bound of the scale factor by taking the squared difference of the first function and the target Chi-squared value, which is 2σ higher than the minimum of the first function.

The goal of these search algorithms is to find an estimate of the surface charge for the hologram data. The calculated surface charge multiplies the COMSOL data uniformly to match the experimental hologram data. The scale factor is directly related to the surface charge value specified in COMSOL.

Therefore, the surface charge on the LDA ice from a hologram is the initial COMSOL surface charge, 1E-5C/m^2, times the scale factor. The calculated scale factor for the phase between the COMSOL and hologram data also applies to the surface charge because equation 2.5 is linear and there is no clear reason to assume an anisotropic charge profile.

The result of this Nelder-Mead simplex application is plotted in Figure 4.2 with the first and second time series data plotted in red and green respectively. The middle four data numbered 5-9 (white) were taken to adjust the hologram properties with the intention of improving contrast and fringe spacing and with no specified time between captures. Unfortunately, that goal was not achieved. The beam was blanked for 10 minutes between hologram 8 and 9 to allow discharge of any built-up charge. The scaled COMSOL surface charge is plotted as the central point surrounded by a rectangle whose top and bottom edge represent the 95% confidence interval value for each time series hologram. The data are plotted in the order that each hologram was taken. The minimum and maximum surface charge of 1.38E-4 and 1.64E-4C/m^2 occur at hologram 10 and 5, respectively. The mean surface charge for all 12 holograms is 1.50E-4 C/m^2. The average height of error bars in Figure 4.2 is 7.32(8)E-5 C/m^2, and the fluctuations from hologram-to-hologram of extracted surface charge yield a 2σ = 1.57(5)E-5C/m^2. Because the fluctuations are approximately five times smaller than the error bar, the charging is in steady-state conditions. A smaller error bar could resolve surface charge time dependence such as shot noise in the charging or beam degradation of the ice.

Figure 4.2

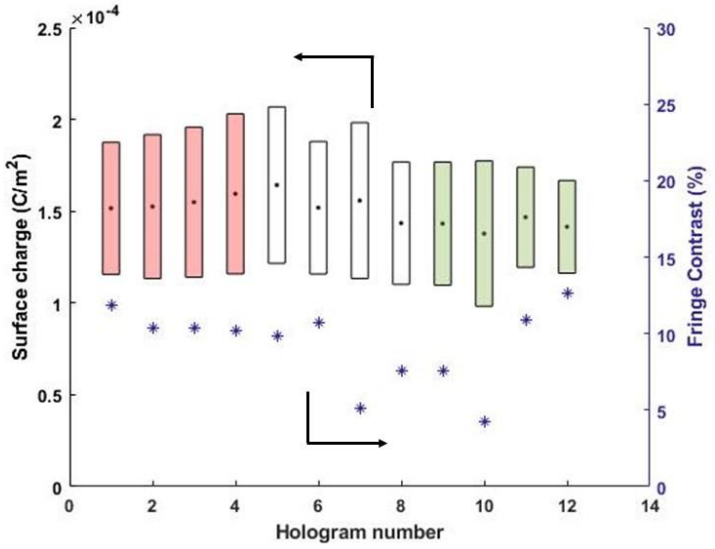

Figure 4.2: The surface charge of LDA ice is plotted for each hologram from the two time series. Red and green indicate the two separate time-series data sets. The central white data are holograms taken to adjust the hologram quality and were not taken at regular time intervals. Surface charge is calculated by multiplication of the phase map scale factor and COMSOL surface charge. The central point is surrounded by a rectangle whose top and bottom edge indicate the calculated 95% confidence interval for each hologram, as described in the text. The fringe contrast of each hologram is plotted using the right y-axis and is represented by asterisks. Exposure times for holograms 1-6 was 4 seconds and 7-12 was 8 seconds.

Since LDA ice is a weak phase object, and the diameter of the hole is large compared to the fringe spacing, the information loss is thus assumed low, and the reconstructed phase map is accurate up to the phase sensitivity. The fringe contrast of each hologram is plotted on the right y-axis and show two general clusters at 10% and 5% roughly. Fringe contrast is a simple and quick way to judge the quality of the hologram through equation 2.14. A complete list of relevant holography parameters for each hologram in the time series is shown in Table 4.1.

Hologram Number	Scale Factor	R-Squared	Eccentricity	Fringe Spacing (nm)	Fringe Contrast (%)	Average Electrons	Sigma-thy (rad)	Sigma-exp (rad)	Voltage max (V)	Voltage Perimeter (V)	Dose (e^-/ Å^2)	Dose Rate (e^-/Å^2/s)
S4-2	15.2	0.899	0.33	27.3	11.9	4350	0.18	0.29	19.0	13.3	1540	390
S4-3	15.3	0.884	0.33	27.4	10.3	4350	0.21	0.31	19.1	13.3	1540	390
S4-4	15.5	0.878	0.31	27.6	10.3	4340	0.21	0.33	19.4	13.6	1540	380
S4-5	15.9	0.870	0.30	26.9	10.2	4340	0.21	0.32	20.0	14.0	1540	380
S5-1	16.4	0.882	0.30	28.5	9.9	5410	0.19	0.34	20.5	14.4	1910	480
S5-2	15.2	0.899	0.31	27.4	10.7	4370	0.20	0.25	19.0	13.3	1550	390
S5-3	15.6	0.872	0.31	27.6	5.1	8790	0.30	0.33	19.5	13.6	3110	390
S5-4	14.4	0.903	0.28	27.7	7.6	8790	0.20	0.27	18.0	12.6	3110	390
S5-5	14.3	0.901	0.26	27.0	7.6	8870	0.20	0.26	17.9	12.5	3140	390
S5-6	13.8	0.859	0.31	27.6	4.2	8840	0.36	0.38	17.2	12.1	3130	390
S5-7	14.7	0.935	0.28	27.3	10.9	8840	0.14	0.18	18.4	12.8	3130	390
S5-8	14.1	0.940	0.27	27.3	12.6	8820	0.12	0.17	17.7	12.4	3120	390

Table 4.1: A complete itemization of all relevant holography parameters for the time series. In section 4.1.2, eccentricity is calculated by identifying the semi-major and semi-minor axes in an image processing program. Average electrons are calculated by scaling the average detector counts by the counts per electron gain from the manufacture and the reconstructed pixel size in phase space.

Even though the fluctuations in extracted surface charge fit within the span of their error bar, showing a 95% confidence interval for uncorrelated errors, it is nevertheless instructive to look for possible correlations within the time series data. Comparisons between sequential holograms in the red and green data sets indicate, at most, 7.9E-5C/m^2 increased charge between hologram 1 and 4, a 5.2% increase. The maximum charge difference of 2.6E-4C/m^2 is a 16.1% decrease between holograms 5 and 10. However, since hologram 5 is from the white data set and 10 from the green, this comparison provides less useful information. Comparing hologram 1 and 5 suggests there might be a steady charging rate during the >8-minute interval. The decrease from hologram 5 to 6 and the continued lower charge values for holograms 6-12 indicates a maximum in surface charge may have occurred at hologram 5 followed by some discharging between 5 and 6 and no further increase in surface charge

thereafter, unlike what is seen between holograms 1-5. Notice that neighboring holograms 8 and 9, taken 10 minutes apart, differ by 0.7% most likely meaning the LDA ice did not discharge during the 10 minutes while the beam was blanked. However, all of these fluctuations are within the 95% confidence interval for uncorrelated errors and thus specific changes in charge density during the time series should be interpreted cautiously.

It is worthwhile discussing the possibility of fluctuations in charge density due to shot noise. The charging fluctuations are estimated as $\sqrt{n}/n$ where n is the number of electrons (in this case holes) that comprise the surface charge on the LDA ice. Counting both surfaces, 6,000 electrons result in a fluctuation noise of 1.3% which is clearly smaller than the variations seen in Figure 4.2. Thus, the origin of the 95% confidence interval is likely from other sources such as the fringe contrast of the hologram and the accuracy of the electrostatic model.

The COMSOL model also produces potentials that are experimentally relevant. The electric potential values at the center and the perimeter of the hole were identified as 1.25V and 0.85V respectively, in the unscaled model. Using the scale factors from Table 4.1 results in a scaled electric potential range of 17-21V and 12-14V, for the center and perimeter, respectively. The average peak potential is 18.8V with a standard deviation $\sigma_V = 0.985V$, a 5% variation, across all 12 holograms. Equation 2.14 calculates the theoretical standard deviation in phase as 0.14-0.38 radians. It is common practice in off-axis electron holography analysis to use the theoretical standard deviation in phase and equation 2.5 to calculate a corresponding electric potential sensitivity[118]. However, for typical holography specimens, the electric potential does not extend past the boundary of the specimen, thus enabling an exact quantification of the extent of the electric potential the electrons interact with, which is the thickness of the specimen. As Figure 3.5C suggests, the electric potential extends well past the

30nm thickness of the LDA ice studied here. Therefore, the standard method to determine the off-axis holography electric potential sensitivity is not applicable in this work because the resulting estimate of electric potential sensitivity is 9-26μV, a significantly better sensitivity than could normally be expected from the other holography parameters. Thus, only the experimental standard deviation in electric potential is discussed.

The experimental standard deviation in phase is calculated by selecting a square region of the unwrapped phase profile within the hole and subtracting a 2D parabolic fit creating a residue plot. The standard deviation of the residue plot is the experimental detection sensitivity with a range from 0.17-0.38 radians, which agrees with the theoretical range from above, 0.14-0.38 radians. This agreement indicates the experimental phase sensitivity nearly achieves the theoretical limit for the given holograms constrained by shot noise and fringe contrast in the data.

At this point there are two important parameters that have not been discussed at length: MIP and camera sensitivity and noise. The reported MIP for LDA ice is 3.5V[76] but does not matter for the COMSOL data because when the sideband is selected, a constant phase shift is removed from the data, thus MIP of LDA ice is not an observable quantity in this holography geometry. As mentioned briefly in chapter 2, the camera is not optimal for holography. According to the camera documentation, the counts/electron recorded by each pixel is between 2-8. A value of 4 was chosen to calculate the electron number in Table 4.1. A binning of 2 was used for the holograms in Table 4.1 as well as the following holograms in section 4.2.

Finally, two means of quality verification are done for the scale factor result. First, the hologram and COMSOL data are co-plotted and visually inspected. With an appropriate scale factor and offset selection, the COMSOL data should intersect near the median of the hologram data inside the hole.

When the hologram data is plotted as points and the COMSOL data as a surface, there does appear to be roughly half the hologram data points above and below the COMSOL data. This could be made rigorous by exactly counting the number of data points above and below which is analogous to creating a residual plot. This method of counting was not done for three main reasons: the visual test is more for subjective quality assessment than rigor, there is subtle complexity with mismatched matrix dimensions and different matrix step sizes between neighboring data points, and R-squared was used as a second quality verification. The R-squared for the entire time series spans 0.859 – 0.940.

4.1.2 Simulation Geometry Corrections

Careful inspection of Figure 4.1F and the co-plotted data of the hologram and COMSOL suggest that the shape of the hole in the a-C film is not circular. By identifying the perimeter of each hole and assuming the semi-minor axis is the same size as the radius of the circle (1μm), the eccentricity was calculated and shown in Table 4.1 with a mean and standard deviation of 0.2984 and 0.0207 respectively. The possible impact of this eccentricity is discussed and other geometric effects.

Assuming the semi-minor axis is 1μm, the area of the ellipse is 3.5-5.7% larger resulting in an underestimation of charge from the COMSOL model. Replacing the 1μm radius circle with an ellipse of the same semi-minor axis and a 5% increase for the semi-major axis in COMSOL results in Figure 4.3A depicting a slice through the center of the phase maps for a circle (black) and an ellipse (red). The vacuum volume is 5μm above and below, ground is only on the exterior perimeter of the a-C, and the surface charge is 1E-5 C/m^2. The peak value percent difference between the circle and ellipse is the same 5% as the area difference. The ellipse COMSOL data set does increase the calculated R-squared value from the Nelder-Mead optimization by roughly 0.01 for each hologram. However, there is the same asymmetry observed from the visual inspection of the analogous residual plot for a circular hole in

the ellipse data. Specifically, hologram phase values are asymmetrically above the COMSOL data in the y direction and below in the x direction when compared with the elliptical COMSOL simulation. Rotation of the ellipse does not resolve the asymmetry. This indicates that while an ellipse is a more accurate model than a circle, there are still other sources of asymmetric phase contribution that are the same order of magnitude or larger.

Figure 4.3

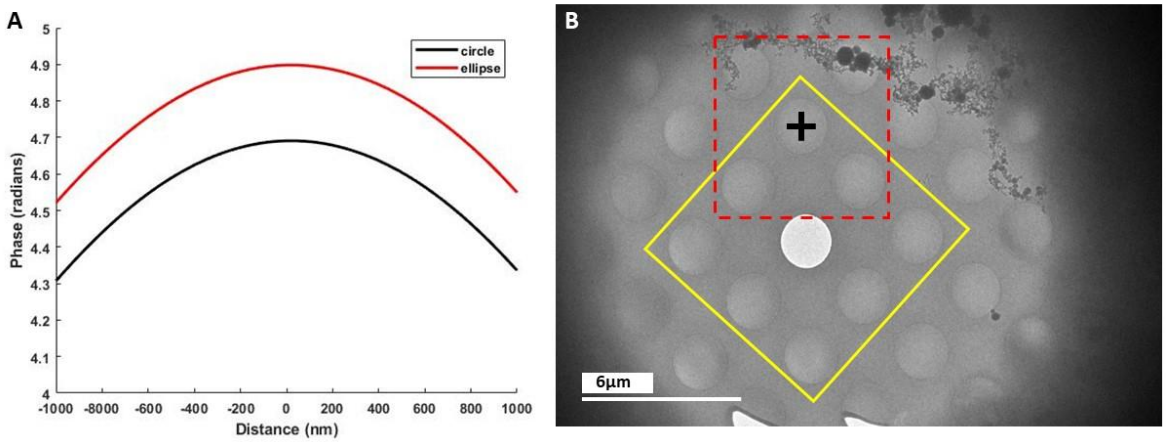

Figure 4.3: The central slice from the COMSOL phase map in (A) shows the phase profile for a circular hole and an elliptical hole with a semi-minor axis equal to the radius of the circle and a 5% increase for the semi-major axis. A low magnification image (B) of the region of interest for holography. The red and yellow boxes indicate the two regions that were simulated in COMSOL. The red boxed region tests the effect of a charged object near the hologram location. The yellow boxed region tests the effect of charge variation of neighboring holes as described below. The black plus sign is the hole measured in both cases.

Another source of possible phase contribution can be seen in Figure 4.3B. At the top right of the image, large ice crystals are located on the surface, likely formed from ambient moisture during specimen transfer into the cryo-holder. Because of the low electrical conductance of ice[149,183–185], these ice crystals can charge and distort the path of the electrons. A five circular hole geometry was implemented in COMSOL shown by the red box in Figure 4.3B. Each hole is identical in dimension, ice thickness, and surface charge. A point charge was placed at the center of a corner hole to simulate the

ice crystal charge and the magnitude of the charge was varied from one electron to 1E-14 C. The electric potential data for the hole with a black plus sign were exported and the previously mentioned analysis and optimization was done. A charge below 1E-17C shifted the profile of the COMSOL integrated potential less than the tolerance of the simulation, 1E-3. When a charge of 1E-16C or larger was applied, the integrated potential peak shifted towards the point charge with increasing shift as the charge increased. At 1E-15C, the integrated potential profile was effectively a linear plane instead of a 2D parabola as the peak occurred at the corner pixel closest to the point charge. Applying a 2D parabola fit to center the peak of the potential and then using the search algorithm resulted in a scale factor of 44.68 and an R-squared of 0.76. These values are significantly worse without the linear plane adjustment and disagree with the experiment. In principle, it is possible that a point charge at a different location relative to the center of the extracted hole could result in a better R-squared value. Also, using a distribution of extended charge spheres to model the charged ice could increase the accuracy of this geometric correction. However, the magnitude of improvement from the modifications tested above indicate this is unlikely when compared to the one-hole model.

A second geometry test was conducted and is represented by the yellow box containing nine holes in Figure 4.3B. A nine circular hole geometry was constructed in COMSOL with identical diameter holes. The central hole was kept empty while the surrounding eight holes were filled with LDA ice. Two surface charge profiles were applied: identical charge and varied charge on each hole. For the identical charge case, 1E-5 C/m^2 was chosen. The varied charge case had charges from 1E-6 to 1E-5 C/m^2 with the intention of breaking symmetry. The electric potential data for both charge profiles were extracted for the same hole as above, indicated by a black plus sign, and the same analysis as previously mentioned was carried out. When a uniform surface charge was applied to all LDA ice filled holes, the

summed potential profile achieved a maximum value at the perimeter of the sampled region (i.e. in the a-C) and is best represented by a linear plane more than a 2D parabola. With the non-uniform surface charge between holes, a skewed 2D parabola represented the summed potential within the sampled region when weaker surface charges flanked the indicated hole. The maximum potential occurred halfway between the center of the hole and the perimeter of the hole at a 45° angle towards the empty hole. Applying a 2D parabola fit to center the peak of the potential and then using the search algorithm resulted in a scale factor of 38.6 and an R-squared of 0.819. These values are significantly worse without the linear plane adjustment. This shows the nine-hole adjustment does not improve the model relative to the data.

A combination of these three geometry modifications—elliptical hole, neighboring charged object, and variation in neighboring surface charges—could improve the overall model. Changing the circular hole geometry to an ellipse in the 5-hole and 9-hole geometries could result in a measurable effect when compared to the simple one-hole model. Other possible simulation considerations such as ice thickness variation, asymmetric charge profile, membrane deflection, a-C variation, and others likely would improve the accuracy of our model. However, given the minimal improvement from any one of the tested configuration changes and previous justifications given in Chapter 2 and 3, the possible improvement is at best a 40% reduction to the 95% confidence interval of charge density. This would not modify any conclusions described above. Another separate origin for the observed elliptical shape could result from geometric distortions due to inherent imperfections of electron lenses. A detailed description can be found in Hawkes and Kasper's *Principles of Electron Optics*.

A few final words on the application of the Nelder-Mead simplex optimization algorithm. From the theory of off-axis electron holography, equation 2.5 does not provide a direct path to calculate the

surface charge. Solving Maxwell's equations for the geometry would provide a direct path to take the electric potential map and convert that into a surface charge. However, the integrals involved do not have closed-form solutions so custom numerical methods are required, which is not significantly different than the COMSOL approach used above. Given this, few options remain to determine the surface charge aside from the comparative method outlined above. The resulting scale factor returns an estimate of the exact surface charge from each hologram and the values are justified. It is not clear that there is an alternate method to directly measure the surface charge on ice under electron radiation. Others[185,187] have estimated the potential difference between the edge and middle of a similar LDA filled hole using defocus contrast, but the technique used here is more widely accepted as a method to directly measure the electromagnetic potential of a specimen.

Cryo-EM specimens of vitreous DI water were imaged with off-axis electron holography to determine the surface charge state of the LDA ice. A total of 12 holograms were taken with an experimental phase sensitivity of 0.17 – 0.38 radians. A representative COMSOL model was used to extract a surface charge scale factor from the hologram data. A surface charge of 1.5E-4 ± 1.6E-5 C/m^2, due to secondary electron emission, for 2μm x 30nm circular holes filled with LDA ice was calculated by use of a Nelder-Mead simples search algorithm.

4.2 Mean Inner Potential of Gold Nanoparticles

One of the main goals for this research is to better understand the behavior of ions at charged interfaces and under extreme confinement. To that end, the addition of a charged nanoparticle into a weak electrolyte solution is an ideal system to study. As has been shown in Chapter 2 and the previous section of this chapter, the sensitivity requirement to detect phase shifts from 1.5E-4C/m^2 are at least $\pi/10$ radians. Therefore, reducing the total charge, electron interaction area, and adding ionic screening

necessitate either an improved geometry, improved lens configuration and/or an improved electron detection system. The limitations from the geometry and TEM did not prevent initial investigations of charged nanoparticles in DI water and measurement of the MIP.

4.2.1 Holograms of Charged Nanoparticles

Cryo-EM specimens were made by replacing pure DI water with 1.067nM solution of NanoPartz functionalized gold nanocubes as discussed in Chapter 2. Nanocubes were chosen in an initial attempt to detect ion ordering at the solid-liquid interface shown by the Majumdar group[200] with a larger, 1nm, ion. However, the Rose criteria detection limit[63,201] prevents imaging of smaller ions such as typical monatomic solutes. The Rose criteria says that a detector can resolve an object with a SNR > 3-5. Therefore, off-axis holography was chosen as the preferred characterization method. Previously mentioned cryogenic specimen fabrication challenges are compounded by the addition of nanoparticles.

The lack of control for nanoparticle placement within a hole was a further complication to finding ideal locations on a given specimen for holography to be implemented. Nanoparticle location, typically at the edge of a hole, and the average number of nanoparticles per hole led to many specimens with ideal LDA ice quality and filled to empty proximity being discarded because either too many or no nanoparticles occupied filled holes. For a 2μm hole, fewer than 20 nanoparticles contained within was considered acceptable. Minimal aggregation, reasonable spacing, and reasonable distance from the hole edge were the primary metrics that were applied when looking for ideal locations. Representative filled holes shown in Figure 4.4 A, B were taken on Quantifoil R2/2 and C,D were taken on holey carbon. Figure 4.4A,B were taken using FLC setting 10 shown in Table 4.2, 6kx for C, and 3kx for D.

FLC Setting 10			
OM	0000	IL1	0000
OL-C	2000	IL2	FFFF
OL-C	0000	IL3	E6FF
OM	BF0B	PL	FFFF

Table 4.2: Free Lens Control setting 10 used to acquire Figure 4.4A,B.

Figure 4.4

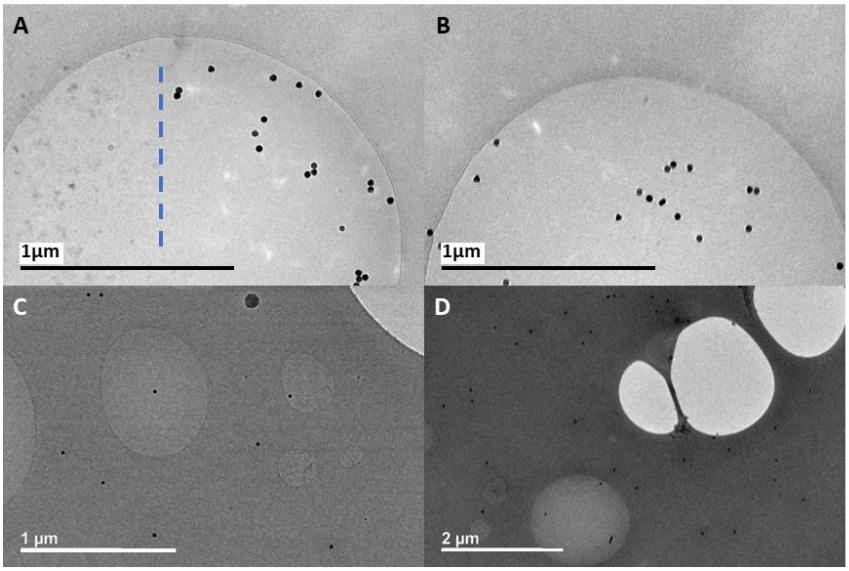

Figure 4.4: Representative images of dispersed nanoparticles in LDA ice on Quantifoil R2/2 (A,B) and holey carbon (C,D). Both pairs were acquired from the same specimen in the same session.

In Figure 4.4A, the blue dashed line roughly separates the left side region where, due to beam damage and heating, the amorphous ice has begun to crystalize. In contrast to this crystallization, the right side of Figure 4.4A and the entirety of Figure 4.4B are still LDA ice with no obvious crystalized region. Some locations to the right of the blue line in A satisfy the Bragg condition and appear in strong contrast to their surrounding ice as well in B. While Figure 4.4A has reduced astigmatism over B, both are not at ideal defocus and contain diffraction contrast from the contained and surrounding nanoparticles. A total of 20 nanoparticles are shown in Figure 4.4A and 18 in B, but A is considered more optimal for holography because of the reduced astigmatism and nanoparticle spread even though a majority of nanoparticles in B are further from the edge of the hole.

An ideal nanoparticle scenario is shown in Figure 4.4C, where a single nanoparticle occupies a filled hole in close proximity to an empty hole at the top right. Though not as ideal, Figure 4.4D contains a filled hole with five nanoparticles where three are clustered and separated from the remaining nanoparticles. This type of distribution in Figure 4.4D is beneficial, allowing for a hologram to measure an isolated nanoparticle such as in Figure 4.4C and a small cluster at the same time in the same hole ostensibly under the same ice conditions. Holograms of Figure 4.4C, D were taken but did not have sufficient contrast and fringe density to measure a strong phase object such as Au, therefore the nanoparticles in each hole were not detected in the wrapped phase map.

The electron hologram of Figure 4.4A is shown in Figure 4.5B. Notice that overlap between the neighboring hole is not complete. Incomplete overlap such as this is acceptable and does not negatively impact the quality of the hologram because any curvature in the phase profile from the charge density of one hole is canceled out by the phase shift of the charge density from the opposing hole. This cancelation is seen in Figure 4.5D where the areas of overlapping LDA ice are nearly flat. Also notice that overlap occurs between two filled holes as evidenced by the addition of two extra nanoparticles that were not seen in Figure 4.5A and fall within the observed perimeter of the overlapping hole marked by blue arrows. As discussed in chapter 2, there are two types of overlap for holography: filled-empty and filled-filled, termed “difference holography”. The main downside to filled-filled overlap is any non-uniformity between the filled holes can result in additional phase shift and phase noise measured by the hologram. In the following analysis, the regions where these two neighboring holes overlap under the biprism are assumed to be ideal LDA ice of identical thickness. One final note is that the surface charge results carried out in chapter 4.1 are not relevant because both filled holes are assumed to effectively

have the same surface charge. Therefore, no additional complexity is added because the surface charge contributions from each hole cancel out any relative phase shift.

Figure 4.5

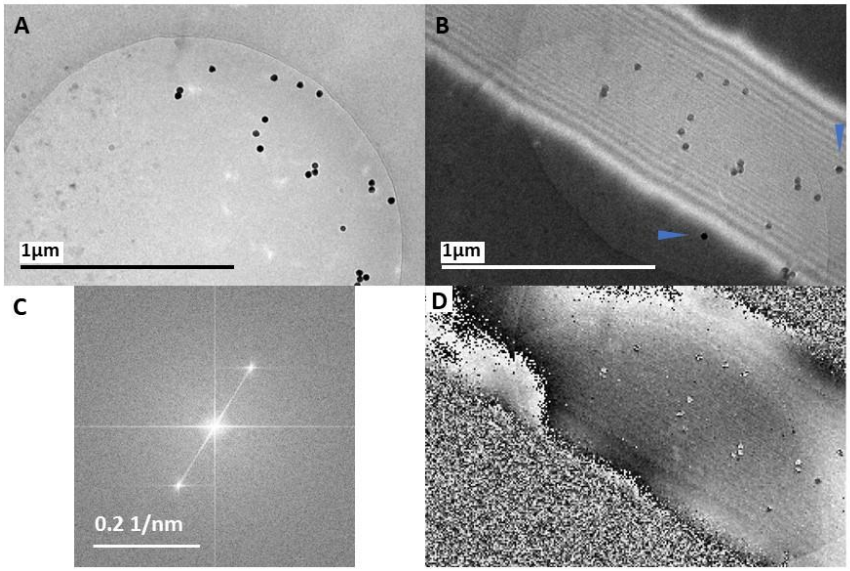

Figure 4.5: Dispersed nanoparticles in LDA ice (A) are overlapped with a neighboring filled hole creating an electron hologram (B). The hologram is Fourier transformed (C) and the wrapped phase map is generated (D) which shares the scale bar in (B).

The Fourier transform of Figure 4.5B is shown in C and the wrapped phase map generated by selecting the top right sideband in C with $\pi/4$ rotation is shown as Figure 4.5D. Comparison between Figure 4.1C and Figure 4.5C demonstrates the affect beam coherence has on the Fourier transform. A clear demonstration of the lack of phase information outside the extent of the hologram is evident by the noise speckle in Figure 4.5D. The unwrapped phase map for Figure 4.5D is shown in Figure 4.6C and Figure 4.5B, D are rescaled for easier investigation in Figure 4.6.

The two most notable features in Figure 4.6B, C are the near inability of the hologram to detect the nanoparticle denoted by the orange arrow in Figure 4.6 and the variations in phase shifts across many of the nanoparticles. The most likely cause for the nanoparticle to barely appear in the wrapped phase map is being at the minimum for hologram pixel density and low fringe density over the

nanoparticle for strong phase objects. Since Au is a strong phase material at this size ($\Delta\phi \sim 2\pi$) and the 6.5nm fringe spacing means at best 5 fringes cover a nanoparticle, significant phase detection errors are more likely to occur at the resolution boundary. From chapter 2, a minimum of 12 hologram pixels are required per reconstructed phase pixel for strong phase objects. Figure 4.6A has 30-40 pixels per nanoparticle which means the accuracy of reconstructed pixel density on a nanoparticle in D should be roughly 3 pixels. The effect of just barely satisfying the strong phase pixel condition is additional uncertainty in the final analysis, in the form of a phase error.

The second notable observation are phase shifts across many of the nanoparticles in B. This visible phase shift on a nanoparticle is obvious when comparing the two nanoparticles labeled 3 and 4 in B. The phase shift cannot come from an unwrapping error, though the shift does affect the accuracy of the unwrapping, because B is the wrapped phase. Therefore, the visible phase shift on some of the nanoparticles is attributed to fringe shifts across the nanoparticle. As a fringe crosses the water-gold interface, a shift occurs proportional to the phase shift. If the shift is large enough, the shifted fringe can overlap onto a non-shifted fringe leaving behind a region on the nanoparticle not covered by a fringe. This change in fringe spacing on the nanoparticle results in a loss of information represented in the wrapped and unwrapped phase map as variation in the phase. This can cause a particle to disappear in the phase map.

A third observation is the retention of fringe lines in the wrapped and unwrapped images, attributed to the Fresnel fringes being at a similar period and frequency to the hologram fringes. These Fresnel fringes cannot be corrected for by taking a background reference hologram of just vacuum with the same beam conditions. A reference hologram was not taken for two reasons: 1) the TEM grid is not designed to have a large vacuum region and 2) insufficient detailed recording of beam conditions for the

recorded holograms to go back and recreate near similar conditions later on a different specimen. The main reason for a reference hologram of neighboring vacuum is to subtract phase distortions from the biprism and microscope, and thus these artifacts remain in the data. Nevertheless, for both chapter 4.1 and 4.2 holograms, there does not appear to be any abnormal phase behavior. The addition of reference holograms remains a possible improvement for future work.

Figure 4.6

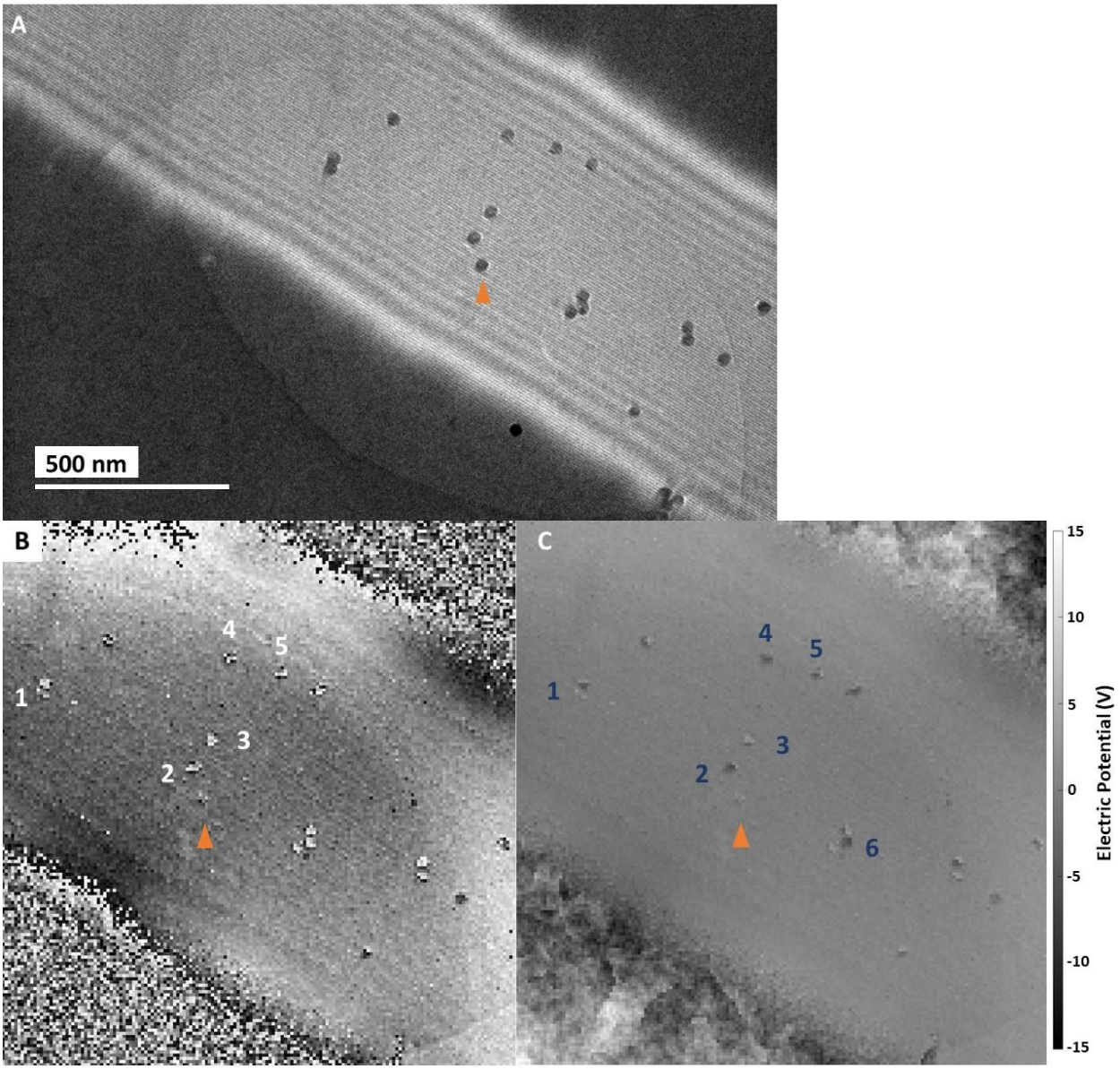

Figure 4.6: Electron hologram (A) wrapped phase map (B) and unwrapped phase map (C) of a give cryo-specimen with nanoparticles dispersed throughout the overlapped region. The dimensional scale for (B,C) are the same.

As mentioned previously in this chapter and chapter 3, phase unwrapping errors are difficult to prevent. Not only will these errors result in an overall incorrect sign for a nanoparticle, but also regions of a nanoparticle that start with a similar value can result in a mixed sign after unwrapping, shown by

comparison of nanoparticles labeled 1 and 3 in Figure 4.6C. As well, comparing the profile of particles 3 and 4 in B to their unwrapped profile in C (same labeled particles) shows that a poor starting condition in nanoparticle 4 can still result in a well unwrapped, correct sign phase value. The exact opposite occurs in particle 3 where unwrapping incorrectly assigns a positive phase shift.

Of all the unwrapping errors encountered, the worst to understand and attempt to fix is when a nanoparticle starts with a poor wrapped phase profile and ends with a similarly poor unwrapped profile as indicated by particle 5 in B and C. This particular nanoparticle profile starts, in B, at the top with a weak value near the background, increases to a stronger positive value at the middle, and ends with a sharp decrease to a negative value which is mirrored in C. Further comparing particle 5 in A shows the aforementioned fringe shifting that when coupled with a strong phase object at the fringe required minimum can lead to unwrapped phase ambiguity. For this particular hologram, there are nanoparticles, 4 and 6, that unwrap with a clear phase profile and sign so phase ambiguity can be resolved for all nanoparticles, but in a less desired and cumbersome manner. Holograms with no correctly unwrapped nanoparticles are more challenging to resolve, but the phase shift for these nanoparticles is expected to be negative.

In the end, the primary complexity is determining the extent of the nanoparticle phase profile: where does the phase shift from the nanoparticle end and the LDA ice phase begin. To reduce input error and bias, an averaging algorithm was created for selected nanoparticles. Eight nanoparticles in Figure 4.4A and ten in Figure 4.4B were selected from the holograms for these original images, and the same algorithm is applied to both sets. An 11-pixel square region surrounding each nanoparticle center was selected and had the phase value at each pixel adjusted to account for phase unwrapping errors. The 11-pixel square had a plane subtracted created by fitting the 40 perimeter pixels of each square. The

mean and standard deviation of the perimeter was calculated and used to create a threshold that each pixel was measured against for phase correction. The threshold condition was mean plus two times the standard deviation. The plane subtraction resulted in the mean being essentially zero, of order 1E-16 radians, as intended so the phase adjustment solely relies on the standard deviation which is a measure of the phase sensitivity. The phase shift from the nanoparticle is expected to be negative, so any pixel larger than the threshold would have 2π subtracted from the phase value. The average phase profile was computed by summing the original orientation, each 90° rotation, and the improper rotation, that is a horizontal flip, increasing the total data size by a factor of eight. Because the orientation of the nanoparticles is arbitrary, the rotation averaging is statistically allowed and analogous to techniques from structural biology in reconstructing proteins. The results for the two holograms are shown in Figure 4.7.

Figure 4.7

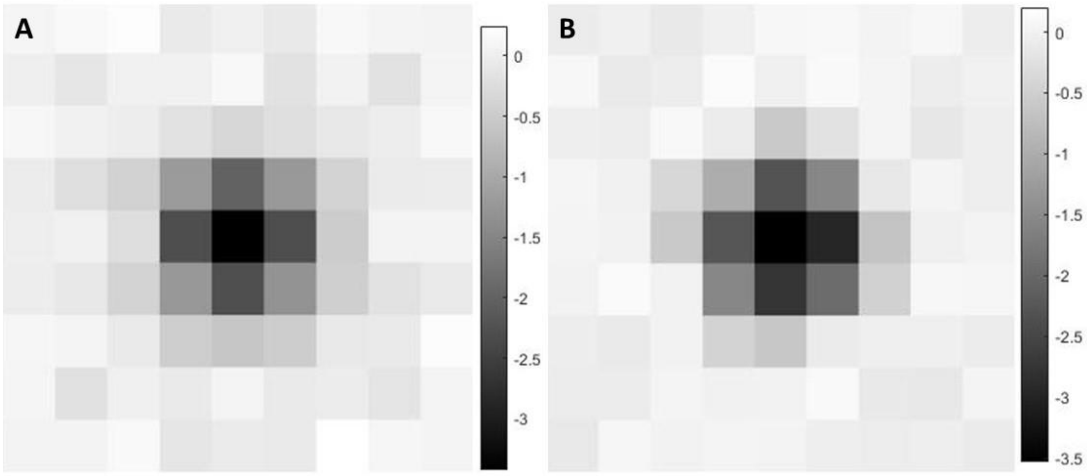

Figure 4.7: Corrected phase maps in radians summed and averaged over eight (A) and ten (B) nanoparticles.

The maximum phase values from each averaged data set are 3.42 and 3.53 radians which converts into 18.8V and 19.4V for the MIP difference of the gold nanoparticle and an identical volume

of LDA ice for Figure 4.7A and B respectively. Correcting for the MIP of LDA ice, the measured MIP of the Au nanoparticles is 22.3V and 22.9V respectively. These values fall within the range of reported values of 21-23V[73,202,203] for Au. The experimental phase detection sensitivity, calculated the same as in chapter 4.1, is 0.45 radians for both A and B and corresponds to a voltage sensitivity of 2.47V. The SNR for these holograms is 7.5 where the noise value is the phase standard deviation from equation 2.14. The optimal thickness for Au in holography from equation 2.32 is 168nm[204] which is 7 times larger than the nanoparticles used. The nanoparticles used are above the MIP transition size of 5nm, wherein decreasing nanoparticle size can double the measured MIP for Au nanoparticles[202].

Assuming orientation of the rod is not an issue, a thicker membrane is required to allow for a 168nm particle to orient parallel to the electron path. The additional specimen thickness will impact the ability of the cryogen to cool the specimen and solution fast enough to allow for uniform LDA ice formation. From a measurement perspective, difference holography would be preferred over vacuum-specimen overlap to eliminate charging affects and the ice contribution. However, confirming the ice thickness is nearly identical for difference holography to work well and the increased radiation damage that is proportional to specimen thickness would impact the quality of the LDA ice and the measurable phase. In short, increasing the Au thickness by more than a factor of two would introduce more challenges than the added thickness solves. The primary improvements for measuring the MIP of Au as a nanoparticle would be increased fringe density on the nanoparticle, increased contrast, more uniform nanocubes, and a large selection of hologram data.

4.2.2 Poisson-Boltzmann Simulation

A primary goal of this dissertation work is to characterize ionic distributions caused by a charged surfaces in electrolytes. This goal was rather lofty considering the starting point and the tools available.

Challenges and limitations in specimen fabrication, specimen optimization, and data collection were present at every step. The limitations became especially apparent when nanoparticles were introduced into the solution and the phase sensitivity was 0.45 radians, similar to that of the LDA ice holograms, but for strong phase objects.

The phase sensitivity required to measure the MIP for a nanoparticle should be better than $1/3^{rd}$ the expected phase shift. For Au, this means a phase sensitivity better than 1.3 radians is necessary and was achieved. The phase sensitivity required to measure the 6V shift from edge to center in LDA ice due to surface charging is 0.45 radians assuming 30nm effective range of the potential, shown above to be unphysical. The achieved sensitivity of 0.17-0.38 radians is comparable to the unphysical 0.43 radian sensitivity indicating that a more accurate effective range of the potential will result in a larger sensitivity threshold. A next question is, assuming surface charging from the electron beam can be ignored or accounted for, what is the phase shift from the arrangement of ions in proximity to a charged surface and over what length scale? To address this question, a discussion of experimental design is necessary.

There are two steps required to determine the phase shift sensitivity for a charged nanoparticle in an electrolyte that is not simply pure water with H^+ and OH^-. First, an electrolyte and concentration range must be determined that retain nanoparticle suspension and will not negatively impact holography and TEM requirements. Second, the surface charge must be measured from the LDA electrolyte with no nanoparticle in solution. Measurement of the electrolyte surface charge is helpful but can be skipped if difference holography is used. To simplify the above chemistry requirements, pure water is chosen as the initial 'electrolyte'. Two possible next electrolytes would be a simple salt such as NaCl and a more complicated, but an easier to detect salt such as $Lu(NO_3)_3$ or $LuCl_3$ were considered[205–207].

The simpler NaCl option would be straightforward in determining a working concentration range but would be harder to detect and keep the nanoparticles in suspension. The lutetium alternatives would be overall more complex. The chemistry would be somewhat more complicated than NaCl and there would be the added challenge of determining how the 3+ ion would arrange on the nanoparticle, especially at edges and vertices. The chemistry calculations were done for NaCl and $Lu(NO_3)_3$ but implementation was unsuccessful due to either incorrect solution calculations, incorrect solution mixing, or poor choice of electrolyte. For these reasons, and for simplicity, water is used as the foundation to discuss experimental feasibility as follows.

To assist with modeling of experimental design, the 2D axisymmetric COMSOL model was used to determine the concentration profile, phase map, and electric potential expected from a charged nanoparticle in water as described in chapter 3 with the results of the simulation plotted in Figure 4.8. The dissociated protons in the DI water will naturally attract to the negative surface of the nanoparticle screening the total charge to some extent. When the exact surface charge of $3e^-/nm^2$ is used, the proton concentration at the edge of the nanoparticle is unreasonably large, 1E57, as expected because the model breaks down at very high concentrations and high surface charge. An effective, screened surface charge was determined by comparing the potential value at two distances from the surface of the nanoparticle to the Zeta potential of the nanoparticle, -31mV. The two distances were 2.5nm and 15nm which are analogous to the hydrodynamic radius[208,209]. With this condition set, the effective surface charge was scaled by 1.3-1.6E-3 to satisfy the potential at the specified hydrodynamic distances.

Figure 4.8

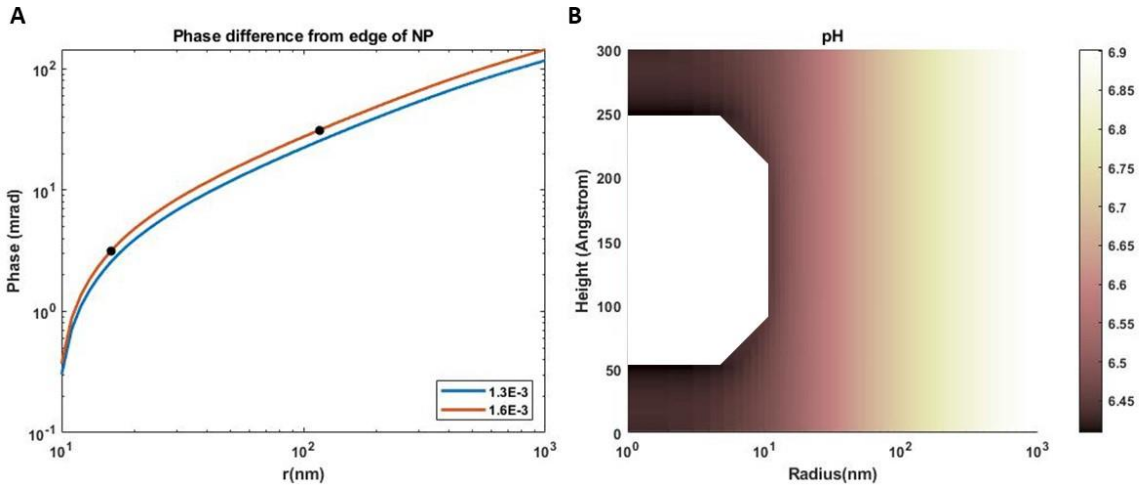

Figure 4.8: The phase difference relative to the edge of the nanoparticle (A) for the scaled surface charge of the nanoparticle due to ionic screening from the PB model. Asterisks indicate the π/10 (right) and π/100 (left) radian phase value. The pH (B) that results from the predicted H^+ concentration from the PB model with 1.3E-3 scaled surface charge.

The blue and orange curves in Figure 4.8A are the phase differences from the edge of the nanoparticle to the water-a-C interface for the scaled surface charges. The phase shift difference transitions at roughly 30nm into what appears to be a power law dependence of value 0.6. Below 30nm, there is a significantly stronger dependence on distance to the phase shift which is expected as the ion concentration reaches a maximum at the surface of the nanoparticle. Phase values of π/100 and π/1000 radians are marked by black dots and occur at 106 and 6nm respectively. The phase sensitivity from the nanoparticle holograms, 0.24 radians, occurs at roughly 2000nm from the edge of the nanoparticle, which is the diameter of the hole in the experiments. This means that subtracting the MIP for Au from the nanoparticle holograms in the previous section would not allow phase detection of any phase shift due to ionic concentrations. At an improved phase sensitivity of π/100, one of the best reported[124], electric potential information is at best available 106nm from the edge of the Au, which is poor spatial resolution for imaging electrolyte double layers.

Several key factors directly impact the distance at which π/100 radian phase shift occurs. First is the actual model used. Changing the model to include ion-ion interaction, ion-surface interaction, reservoir affects, confinement affects, nanoparticle geometry, and LDA ice thickness will all contribute to a more physical estimation of the phase profile. More complete models exist such as the Poisson-Nernst-Planck (PNP) model but require significantly more input into COMSOL and knowledge of the solution parameters which are not always agreed on and available. This last fact is especially true if a more complex electrolyte were used instead of water. Two other key factors are the simulation program and the study type. COMSOL is unlikely the optimal software to solve for the ionic distribution and potential profile to high precision at under 100nm. As well, a steady-state study was used in COMSOL to reduce computation time and model complexity compared to a time-dependent study.

Regardless of the degree of accuracy of the model, improving the distance at which a π/100 radian phase shift occurs is focusing on the wrong problem. The real problem is that the best phase sensitivity is on the order of π/1000 radians achieved with double biprism, hologram averaging, and higher magnification[210]. Measuring a parameter at the sensitivity limit invites errors and is typically avoided. Therefore, the changes that would need to occur for π/100 radian phase sensitivity to effectively measure a phase shift at sub-nm distance from a charged surface with off-axis electron holography are as follows: an optimized geometry, an optimized surface charge, an optimized solution, and an optimized TEM. All these aspects have been discussed in previous chapters and sections and will be compiled in the following chapter.

Chapter 5: Conclusions and Future Work

The motivating question this dissertation sought to answer is, “Can the electric field of dispersed ions in close proximity to a charged surface be measured with off-axis electron holography in a cryo-EM specimen?” A model system consisting of a weak electrolyte, DI water, and functionalized Au nanoparticles was vitrified forming a suspension of H^+ and OH^- ions in LDA ice. Off-axis electron holography was used to answer this question.

5.1 Conclusions

Off-axis electron holograms of pure DI water and DI-water-suspended nanoparticles were collected, and the phase and voltage sensitivity were calculated. The solutions were cryo-plunge frozen on Quantifoil TEM grids, loaded into a Gatan 914 cryo-holder, inserted into a JEOL 2100F, and holograms were collected with a Gatan Orius SC 1000A camera. An experimental phase sensitivity between 0.17-0.38 radians was observed for DI water holograms. The surface charge from secondary electron emission was calculated to range from 1.38-1.64E-4C/m^2 by use of the Nelder-Mead simplex search algorithm comparing experimental holograms to COMSOL simulation phase profiles from a representative specimen geometry. This appears to be the first time a direct measurement of surface charge of LDA ice has been reported. This initial surface charge measurement creates a starting point for further experimental improvement and additive implementation to existing models that utilize LDA ice to reconstruct organic compounds.

The second solution configuration consisting of functionalized Au nanoparticles suspended in DI water resulted in a measured MIP of 22.3 and 22.9V with a phase sensitivity of 0.45 radians and a potential sensitivity of 2.47V for Au. At 25nm, the Au nanoparticles are

nearly 1/7th the ideal holography thickness of 170nm, however, attempting to fabricate a cryo-EM specimen with particles at that scale could introduce vitreous ice degradation among other challenges. Another COMSOL model was created using a 2D-axisymmetric geometry and a modified Poisson-Boltzmann description of the ions to determine the phase sensitivity requirement on off-axis electron holography. Using the phase sensitivity from the MIP holograms, a distance of roughly 2000nm from the nanoparticle was extracted from the simulation where the phase value is the same as the sensitivity indicating an increased phase sensitivity is required to accurately study ion distribution effects with off-axis electron holography.

Using the phase sensitivity as a measure of how close to the nanoparticle surface phase shifts can be observed is a metric to validate the ability of off-axis holography to detect phase shifts from ion concentration. However, this does highlight that increased sensitivity is required to measure the phase shift from ions closer 2000nm from the charged nanoparticle with this specimen configuration. Even at near the best reported phase sensitivity of $\pi/100$ radians, the phase shift occurs 106nm from the surface of the nanoparticle for H^+, which is long compared to the typical lengthscales of interest for electrolyte double layers, in the range to 1-10nm. Therefore, given the sensitivity achieved in these holography experiments and comparing to an ionic distribution model many opportunities remain for observing potentials at single-digit nanometer lengthscales.

5.2 Future Work

The investigation of LDA ice charging and the combination of off-axis electron holography with cryo-EM specimens encountered many challenges. The three most notable and

in need of serious consideration before moving further along this research path are electron detection, specimen geometry, and specimen composition.

5.2.1 Challenge 1: Electron Detection

The CCD camera used to collect these holograms is not optimized for holography mostly due to gain non-linearities. Since its development, it has been surpassed by current CCD offerings and even more so by electron direct detection systems. Given that modern TEM electron detectors are capable of drift correction, rapid detection, single electron counting, flat quantum efficiency, and high gain, repeating these experiments on a TEM with a modern detector would improve fringe contrast, sensitivity, and reproducibility. A change of camera is by far the easiest and most significant change that should be implemented.

5.2.2 Challenge 2: Specimen Geometry

Specimen geometry plays a significant role in off-axis holography. Thickness, composition, orientation, flatness, uniformity, hole size, hole shape, and hole spacing compose the geometry parameter space. The most important on this list are the hole specific parameters. If the hole is too large, serious ice deflection will occur resulting in either a broken ice region or serious thickness uniformity issues. On the opposite side, if the hole is too small in diameter, filling can be an issue. For both, the profile of the ice is the second concern. Thickness variation will introduce phase shifts, by definition of holography, simply because one section of electrons passes through more or less material and are shifted by different amounts. One hole diameter was reported in this dissertation, 2μm, but other diameter holes were tested and measured for thickness uniformity. Each hole diameter was measured flat up to ±1nm. Hole spacing is also

important. Regardless of specimen -vacuum overlap or difference holography, if the intended regions of overlap are not close enough for the biprism to create overlap and retain coherence, nothing else matters. The best resolutions are achieved in holography by spending time optimizing this spacing. This is done by determining the required fringe spacing for the required resolution. Finally, hole shape. This dissertation utilized circular holes but elliptic, square, and hexagonal are alternative options. The shape of the hole impacts ice deflection with hexagonal being the best at reducing this.

Specimen uniformity and composition are closely related both for the support structure and the solution. For the a-C Quantifoil, thickness variations affect the relative phase shift and non-uniform density affects conductivity properties. If there is a conductivity gradient around the perimeter of the hole, non-uniform, charging, discharging, and secondary electron capture will occur adding further complexity to interpretation. Selection of the support structure composition affects drift, buckling, and electric properties. All-gold support structures and films have been shown to reduce drift over Cu and a-C. Like with hole shape, membrane composition can also reduce buckling. Finally, the membrane composition obviously will affect conductivity. Implementing optimized hole shape, hole diameter, membrane composition, and membrane thickness will directly improve drift and signal of the recorded holograms.

5.2.3 Challenge 3: Specimen Composition

The last major challenge is specimen composition. This dissertation focused on DI water because of the simplicity and initial ease of use. Adding solute to water such as NaCl away from the saturation limit at room temperature will not seriously impact the process of plunge freezing to create a vitreous ice. Solutions near the concentration limit might produce challenges for

plunge freezing. Supporting documentation from published literature for these kinetic effects has not been found. Replacing DI water with an organic or ionic solvent is commonly done in structural biology so the solute particle remains in suspension and/or properly dispersed. More exotic solvents would need testing to determine if an amorphous structure forms at LN temperatures.

Increasing the size of the solute from a salt to nanoparticles impacts the relevant physics. Functionalized Au "nanocubes" were chosen because a previous cryo-EM experiment was planned around the flat surfaces of the cubes. The guiding theory was detection of a Stern layer on a sphere would be non-ideal because the curved nature would reduce resolution at the edge and minimize the signal. By choosing a geometry with a flat surface, a properly oriented cube would result in a strong contrast signal from the Au, a small gap where contrast is at a minimum to account for spacing between the surface and Stern layer (and the hydration layers), and a strong contrast increase where the counterion would be tightly bound. This was achieved with larger Keggin ions in a collaboration with the Bazant and Majumdar groups[200]. Imaging of individual elemental ions at relevant concentrations remains out of reach because the required dose for the detector to have enough SNR is well above any effective cryo-EM dose, significantly beyond low-dose standards. Whether imaging of individual elemental ions at lower concentrations or larger ions, such as Keggin molecules, single-particle cryo-electron holography remains an area with abundant opportunities and conducting this work in an optimized system, such as a dedicated cryo-TEM, could enable more progress.

5.2.4 Further Opportunities

Further challenges such as modeling, phase detection limit, drift and exposure, fringe contrast and separation, and coherence exist. Aside from modeling, each of the above are interrelated amongst themselves and to the three primary challenges. Addressing the three primary challenges will reduce the effect or could completely eliminate some of these additional challenges. That is not to say these additional challenges will automatically be resolved by only addressing the primary challenges.

To wit, an increased phase detection limit and phase sensitivity will very clearly enable more detailed investigations of ionic distributions. Achieving a $\pi/100$ radians sensitivity shifts the 86nm distance down to 16nm from the edge of the nanoparticle. Optimizing the geometry and solution choice can also result in better contrast and more substantial phase shifts over shorter distances which would be ideal. By increasing the magnitude of the phase shift, a $\pi/100$ radians sensitivity affords detection of single-digit nanometer separation from a charged surface. At the same time, optimizing the geometry without addressing the detection system or fringe contrast is pulling on one string in a tangled heap.

Improving the camera to a direct detection system affords better detector quantum efficiency and increased gain. Additionally, specimen drift can be accounted for by stitching subsequent holograms together instead of taking prolonged single exposures. Reduced drift results in improved coherence thereby improving the phase sensitivity. Beam coherence limits fringe spacing and contrast. Increasing the biprism voltage will decrease the fringe spacing but at some voltage coherence between the interfered beam paths is rapidly lost. Reduced fringe spacing means finer detail resolution in the reconstructed phase image and therefore better phase

accuracy. The addition of a C_S corrector will reduce the aberrations resulting in several improvements: information limit of the microscope, enhanced signal resolution, increased optical degrees of freedom, crystal tilt replaced by beam tilt, enhanced isoplanacy, and enhanced a posteriori C_S correction[211]. Fringe contrast improvement is described in two ways from equation 2.13 as either normalized intensity difference or a composition of spatial coherence and instabilities of the entire system: camera, specimen, TEM. An improved detector, optimizing specimen thickness, minimizing TEM instabilities, and increasing spatial coherence result in better contrast which leads to better phase sensitivity.

5.2.5 Modeling Opportunities

The last non-primary challenge to improve is the model that the experimental data is compared against. Changing from the current PB model to a more sophisticated one such as PNP or something else will immediately result in a more accurate phase profile for whichever geometry is used. A better, more complex improvement would be optimizing or replacing the model solver, COMSOL, with a better suited method, but this falls outside the scope of this dissertation. Improving model geometry, solution chemistry, solution physics, and model solver could increase the accuracy of the extracted values such as surface charge and phase shift distance as discussed in chapter 4.1 and 4.3 respectively.

5.3 Experimental Opportunities

With improvements to the as-described experiment, the last remaining topic is where these results could be used in the broader scientific community. As stated in chapter 1, the two primary motivations for this work are to improve current cryo-EM reconstruction techniques that

ignore the surface charging affects and measure electromagnetic fields at SDN length scales, possibly with SDN pores.

Figure 4.2 appears to suggest that a reduction in the charge density below 5E-5C/m^2 would make the charging effect non-observable if the error bar remains constant and the observations span zero charge density. However, the error bar is empirically determined, and it might be proportional to the observed field strength. A possible way to investigate this would be to vary the diameter of the Quantifoil holes thus producing a smaller charge density due to shortened diffusion path to ground and comparing the size of the newly observed error bar.

An already contemplated change to the current specimen geometry is repeating these experiments with intentionally thick LDA ice either by under-blotting or by utilizing thicker TEM grids. As described in chapter 4.2, the optimal holography thickness is 5-20 times larger than the 30nm used here. Under-blotting typically leaves all holes completely filled and excess solution nonuniformly dispersed across the surfaces of the grid. Difference holography negates the drawback of all holes being filled. To overcome the thickness nonuniformity, careful planning, calibration, and execution of the blotting technique are required. Some of the earliest cryo-EM work done in this dissertation produced oval shaped regions of LDA ice extending past the hole diameter. At the time, no consideration was given to the possible uses of specimens such as those. The other hidden challenge with thicker ice is the quality of the vitrifying process. If the grid thickness is 100nm for example, will the ice be uniformly LDA or will there be patches of crystalline ice? As well, thicker grids may result in thickness variation even when fully blotted where no excess solution remains on the surfaces and may impact the extent of membrane deflection.

Entirely alternate geometries could be studied instead of the standard TEM grid version. With the large caveat that fabrication of the geometry becomes increasingly challenging and LDA ice quality is suspect, consider a tube of some diameter and length 100-500nm filled with LDA ice. The tube would have intentional neighboring holes to allow for a vacuum signal. Depending on the possible diameter of the hole, investigating ionic ordering, electroneutrality breakdown, and fringe fields could be explored.

As an example, consider the following. In collaboration with the Bazant and Majumdar groups, a first of its kind measurement of discrete Keggin counterions roughly 1nm in diameter at electrically charged solid-liquid interfaces using cryo-EM as achieved. The result agrees well with a weighted density approximation accounting for ion-ion interaction, high surface charge, and high ion valency. The continuation of this collaboration, now including the Strano and Wang groups, aims to measure CNT filling with TEM and Raman. Since the carbon nanotubes have already been a focus for off-axis holography, adding off-axis holography to the measurement of filled CNTs might reveal changes to electric field properties of empty CNTs. In addition, investigating fringe fields at membrane openings and CNT edges maybe be possible with the best sensitivities.

A general assumption in cryogenic TEM specimen fabrication is that the distribution of and within the liquid solution is preserved when vitrified. This assumption was applied throughout this dissertation without pause. By controlling the kinetics during the vitrification process such as through starting temperature, specimen thickness, and the addition of diffusion mediating solutes, it may be possible to explore the kinetics of the vitrification process.

To conclude. An ideal research experiment would be to identify a dedicated cryo-TEM with a biprism and possibly C_S correction and measure ionic distributions in proximity to charged particles. More practically, a more detailed investigation into surface charging of different solvents relevant to structural biology should be conducted. There are perhaps even opportunities to study fields surround magnetic particles in suspension by cryo-electron holography.

In the words of a made-up character, from a game I have played far too much of these past 7 years: “Did you really think this would work?”

Bibliography

1. Burke, J. *FLUORIDATED WATER CONTROVERSY: Unbiased Reference Source & What You Need to Know*. (LULU COM, 2017).
2. Bernoulli, D. *Hydrodynamica, sive de viribus et motibus fluidorum commentarii: opus academicum ab auctore, dum Petropoli ageret, congestum*. (sumptibus Johannis Reinholdi Dulseckeri, 1738). doi:10.3931/e-rara-3911
3. J. Faucher, S. *et al.* Critical Knowledge Gaps in Mass Transport Through Single-Digit Nanopores: A Review and Perspective. *J. Phys. Chem. C* **123**, 21309–21326 (2019).
4. D'Odorico, P. *et al.* The Global Food-Energy-Water Nexus. *Rev. Geophys.* **56**, 456–531 (2018).
5. Elimelech, M. & Phillip, W. A. The future of seawater desalination: Energy, technology, and the environment. *Science (80-.).* **333**, 712–717 (2011).
6. Siwy, Z. S. & Howorka, S. Engineered voltage-responsive nanopores. *Chem. Soc. Rev.* **39**, 1115–1132 (2010).
7. Werber, J. R., Deshmukh, A. & Elimelech, M. The Critical Need for Increased Selectivity, Not Increased Water Permeability, for Desalination Membranes. *Environ. Sci. Technol. Lett.* **3**, 112–120 (2016).
8. Park, H. B., Kamcev, J., Robeson, L. M., Elimelech, M. & Freeman, B. D. Maximizing the right stuff: The trade-off between membrane permeability and selectivity. *Science (80-.).* **356**, 1138–1148 (2017).
9. Patel, S. K. *et al.* The relative insignificance of advanced materials in enhancing the energy efficiency of desalination technologies. *Energy Environ. Sci.* **13**, 1694–1710

(2020).

10. Epsztein, R., DuChanois, R. M., Ritt, C. L., Noy, A. & Elimelech, M. Towards single-species selectivity of membranes with subnanometre pores. *Nat. Nanotechnol.* **15**, 426–436 (2020).
11. Tunuguntla, R. H. *et al.* Enhanced water permeability and tunable ion selectivity in subnanometer carbon nanotube porins. *Science (80-.).* **359**, 792–796 (2018).
12. Lee, C. Y., Choi, W., Han, J. H. & Strano, M. S. Coherence resonance in a single-walled carbon nanotube ion channel. *Science (80-.).* **329**, 1320–1324 (2010).
13. Agrawal, K. V., Shimizu, S., Drahushuk, L. W., Kilcoyne, D. & Strano, M. S. Observation of extreme phase transition temperatures of water confined inside isolated carbon nanotubes. *Nat. Nanotechnol.* **12**, 267–273 (2017).
14. Siria, A. *et al.* Giant osmotic energy conversion measured in a single transmembrane boron nitride nanotube. *Nature* **494**, 455–458 (2013).
15. Abraham, J. *et al.* Tunable sieving of ions using graphene oxide membranes. *Nat. Nanotechnol.* **12**, 546–550 (2017).
16. Zhou, K. G. *et al.* Electrically controlled water permeation through graphene oxide membranes. *Nature* **559**, 236–240 (2018).
17. Siwy, Z., Kosińska, I. D., Fuliński, A. & Martin, C. R. Asymmetric diffusion through synthetic nanopores. *Phys. Rev. Lett.* **94**, 1–4 (2005).
18. Martin, C. R. & Siwy, Z. S. Learning Nature's Way: Biosensing with Syntheic Nanopores. *Science (80-.).* **317**, 331–332 (2007).
19. Daiguji, H. Ion transport in nanofluidic channels. *Chem. Soc. Rev.* **39**, 901–911 (2010).

20. Guan, W. & Reed, M. A. Electric field modulation of the membrane potential in solid-state ion channels. *Nano Lett.* **12**, 6441–6447 (2012).

21. Zhong, Q. & Fourkas, J. T. Optical kerr effect spectroscopy of simple liquids. *J. Phys. Chem. B* **112**, 15529–15539 (2008).

22. Piao, Y. *et al.* Brightening of carbon nanotube photoluminescence through the incorporation of sp 3 defects. *Nat. Chem.* **5**, 840–845 (2013).

23. Kwon, H. *et al.* Molecularly Tunable Fluorescent Quantum Defects. *J. Am. Chem. Soc.* **138**, 6878–6885 (2016).

24. Wu, X., Kim, M., Kwon, H. & Wang, Y. H. Photochemical Creation of Fluorescent Quantum Defects in Semiconducting Carbon Nanotube Hosts. *Angew. Chemie - Int. Ed.* **57**, 648–653 (2018).

25. Danné, N. *et al.* Ultrashort Carbon Nanotubes That Fluoresce Brightly in the Near-Infrared. *ACS Nano* **12**, 6059–6065 (2018).

26. Wu, X., Kim, M., Qu, H. & Wang, Y. Single-defect spectroscopy in the shortwave infrared. *Nat. Commun.* **10**, 2672 (2019).

27. Brozena, A. H., Kim, M., Powell, L. R. & Wang, Y. H. Controlling the optical properties of carbon nanotubes with organic colour-centre quantum defects. *Nat. Rev. Chem.* **3**, 375–392 (2019).

28. Kulik, H. J., Schwegler, E. & Galli, G. Probing the structure of salt water under confinement with first-principles molecular dynamics and theoretical X-ray absorption spectroscopy. *J. Phys. Chem. Lett.* **3**, 2653–2658 (2012).

29. Pham, T. A. *et al.* Salt Solutions in Carbon Nanotubes: The Role of Cation-π Interactions.

J. Phys. Chem. C **120**, 7332–7338 (2016).

30. Pham, T. A., Ogitsu, T., Lau, E. Y. & Schwegler, E. Structure and dynamics of aqueous solutions from PBE-based first-principles molecular dynamics simulations. *J. Chem. Phys.* **145**, (2016).

31. Joseph, S. & Aluru, N. R. Hierarchical multiscale simulation of electrokinetic transport in silica nanochannels at the point of zero charge. *Langmuir* **22**, 9041–9051 (2006).

32. Govind Rajan, A., Sresht, V., Pádua, A. A. H., Strano, M. S. & Blankschtein, D. Dominance of Dispersion Interactions and Entropy over Electrostatics in Determining the Wettability and Friction of Two-Dimensional MoS2 Surfaces. *ACS Nano* **10**, 9145–9155 (2016).

33. Misra, R. P. & Blankschtein, D. Insights on the Role of Many-Body Polarization Effects in the Wetting of Graphitic Surfaces by Water. *J. Phys. Chem. C* **121**, 28166–28179 (2017).

34. Storey, B. D. & Bazant, M. Z. Effects of electrostatic correlations on electrokinetic phenomena. *Phys. Rev. E - Stat. Nonlinear, Soft Matter Phys.* **86**, 1–11 (2012).

35. Biesheuvel, P. M. & Bazant, M. Z. Analysis of ionic conductance of carbon nanotubes. *Phys. Rev. E* **94**, 78–81 (2016).

36. Bhadauria, R. & Aluru, N. R. Multiscale modeling of electroosmotic flow: Effects of discrete ion, enhanced viscosity, and surface friction. *J. Chem. Phys.* **146**, (2017).

37. Barati Farimani, A. & Aluru, N. R. Existence of Multiple Phases of Water at Nanotube Interfaces. *J. Phys. Chem. C* **120**, 23763–23771 (2016).

38. Epsztein, R., Shaulsky, E., Dizge, N., Warsinger, D. M. & Elimelech, M. Role of Ionic

Charge Density in Donnan Exclusion of Monovalent Anions by Nanofiltration. *Environ. Sci. Technol.* **52**, 4108–4116 (2018).

39. Wollman, A. J. M., Nudd, R., Hedlund, E. G. & Leake, M. C. From Animaculum to single molecules: 300 years of the light microscope. *Open Biol.* **5**, 150019 (2015).

40. Ruska, E. & Knoll, M. Die magnetische Sammelspule für schnelle Elektronenstrahlen. *Zeitschrift für Tech. Phys.* **12**, 389–400 (1931).

41. Knoll, M. & Ruska, E. Das Elektronenmikroskop. *Zeitschrift für Phys.* **78**, 318–339 (1932).

42. Busch, H. Berechnung der Bahn von Kathodenstrahlen im axialsymmetrischen elektromagnetischen Felde. *Ann. Phys.* **386**, 974–993 (1926).

43. Williams, D. B., Carter, C. B., Williams, D. B. & Carter, C. B. *Transmission Electron Microscopy: Books 1-4. Transmission Electron Microscopy* (1996). doi:10.1007/978-1-4757-2519-3_6

44. Hosokawa, F., Sawada, H., Kondo, Y., Takayanagi, K. & Suenaga, K. Development of Cs and Cc correctors for transmission electron microscopy. *Microscopy* **62**, 23–41 (2013).

45. Faruqi, A. R., Cattermole, D. M., Henderson, R., Mikulec, B. & Raeburn, C. Evaluation of a hybrid pixel detector for electron microscopy. *Ultramicroscopy* **94**, 263–276 (2003).

46. Milazzo, A. *et al.* Active pixel sensor array as a detector for electron microscopy. *Ultramicroscopy* **104**, 152–159 (2005).

47. Swanson, L. W. & Schwind, G. A. Review of ZrO/W Schottky Cathode. in *Handbook of Charged Particle Optics* 28–57 (2009).

48. Mollenstedt, G. & Duker, H. Beobaehtungen und Messungen an Biprisma-lnterferenzen

mit Elektronenwellen. *Zeitschrift fur Phys.* **145**, 377–397 (1956).

49. Saka, H., Kamino, T., Ara, S. & Sasaki, K. In Situ Heating Transmission Electron Microscopy. *MRS Bull.* **33**, 93–100 (2008).

50. Crewe, A. V, Wall, J. & Langmore, J. Visibility of Single Atoms. *Science (80-.).* **168**, 1338–1340 (1970).

51. Bursill, L. A. & Smith, D. J. Interaction of small and extended defects in nonstoichiometric oxides. *Nature* **309**, 319–321 (1984).

52. Colliex, C. *et al.* Capturing the signature of single atoms with the tiny probe of a STEM. *Ultramicroscopy* **123**, 80–89 (2012).

53. Yip, K. M., Fischer, N., Paknia, E., Chari, A. & Stark, H. Atomic-resolution protein structure determination by cryo-EM. *Nature* **587**, 157–161 (2020).

54. Herzik, M. A., Wu, M. & Lander, G. C. High-resolution structure determination of sub-100 kilodalton complexes using conventional cryo-EM. *Nat. Commun.* 489898 (2018). doi:10.1101/489898

55. Herzik, M. A., Wu, M. & Lander, G. C. Achieving better-than-3-Å resolution by single-particle cryo-EM at 200 keV. *Nat. Methods* **14**, 1075–1078 (2017).

56. Glaeser, R. M. How good can cryo-EM become? *Nat. Methods* **13**, 28–32 (2016).

57. Sugimori, Y., Miyata, T., Hashiguchi, H., Okunishi, E. & Mizoguchi, T. Atomic-scale investigation of the heterogeneous structure and ionic distribution in an ionic liquid using scanning transmission electron microscopy. *RSC Adv.* **9**, 10520–10527 (2019).

58. Prabhudev, S. & Guay, D. Probing electrochemical surface/interfacial reactions with liquid cell transmission electron microscopy: a challenge or an opportunity? *Curr. Opin.*

Electrochem. **23**, 114–122 (2020).

59. Ross, F. M. Opportunities and challenges in liquid cell electron microscopy. *Science (80-.).* **350**, (2015).

60. Miyata, T. & Mizoguchi, T. Observation of Single Atoms in Liquid and Liquid Inhomogeneous Structures. *Microsc. Microanal.* **22**, 852–853 (2016).

61. Leenheer, A. J., Sullivan, J. P., Shaw, M. J. & Harris, C. T. Leenheer, 2015, A Sealed Liquid Cell for In Situ Transmission Electron Micorsocpy of Controlled Electrochemical Processes. *J. Microelectromechanical Syst.* 1–8 (2014).

62. Park, J. *et al.* Direct observation of nanoparticle superlattice formation by using liquid cell transmission electron microscopy. *ACS Nano* **6**, 2078–2085 (2012).

63. de Jonge, N., Houben, L., Dunin-Borkowski, R. E. & Ross, F. M. Resolution and aberration correction in liquid cell transmission electron microscopy. *Nat. Rev. Mater.* **4**, 61–78 (2019).

64. Wang, Z. L., Poncharal, P. & De Heer, W. A. Nanomeasurements of individual carbon nanotubes by in situ TEM. *Pure Appl. Chem.* **72**, 209–219 (2000).

65. Branca, C. *et al.* Structural and vibrational properties of carbon nanotubes by TEM and infrared spectroscopy. *Diam. Relat. Mater.* **13**, 1249–1253 (2004).

66. Chao, H.-Y., Jiang, H., Cumings, J. & Sharma, R. In-Situ Measurements of Single Walled Carbon Nanotube Growth Reveal the Structures of Active and Inactive Catalyst Nanoparticles . *Microsc. Microanal.* **25**, 1452–1453 (2019).

67. Lin, Y. *et al.* Carbon-Nanotube-Encapsulated-Sulfur Cathodes for Lithium-Sulfur Batteries: Integrated Computational Design and Experimental Validation. *Nano Lett.* **22**,

441–447 (2022).

68. Liu, X. H. & Huang, J. Y. In situ TEM electrochemistry of anode materials in lithium ion batteries. *Energy Environ. Sci.* **4**, 3844–3860 (2011).

69. Wu, F. & Yao, N. Advances in sealed liquid cells for in-situ TEM electrochemial investigation of lithium-ion battery. *Nano Energy* **11**, 196–210 (2015).

70. Nagayama, K. & Danev, R. Phase contrast electron microscopy: Development of thin-film phase plates and biological applications. *Philos. Trans. R. Soc. B Biol. Sci.* **363**, 2153–2162 (2008).

71. Volkl, E., Allard, L. F. & Joy, D. C. *Introduction to Electron Holography*. (1999).

72. Yesibolati, M. N. *et al.* Mean Inner Potential of Liquid Water. *Phys. Rev. Lett.* **124**, 18–22 (2020).

73. Goswami, A. & Lisgarten, N. D. The measurement of inner potentials for copper, silver and gold. *J. Phys. C Solid State Phys.* **15**, 4217–4223 (1982).

74. Auslender, A. *et al.* Mean inner potential of graphite measured by electron holography: Probing charge distribution and orbital diamagnetic susceptibility. *Carbon N. Y.* **179**, 288–298 (2021).

75. Winkler, F. *et al.* Quantitative measurement of mean inner potential and specimen thickness from high-resolution off-axis electron holograms of ultra-thin layered WSe2. *Ultramicroscopy* **178**, 38–47 (2017).

76. Harscher, A. & Lichte, H. Inelastic mean free path and mean inner potential of carbon foil and vitrified ice measured with electron holography. *ICEM14, Cancun, Mex.* **31**, 553–554 (1998).

77. Cooper, D., Pan, C. T. & Haigh, S. Atomic resolution electrostatic potential mapping of graphene sheets by off-axis electron holography. *J. Appl. Phys.* **115**, (2014).

78. Tonomura, A. . *Electron holography*. *Springer* (Springer, 1999).

79. Simon, P. *et al.* Electron holography on beam sensitive materials: Organic polymers and mesoporous silica. *Chem. Mater.* **14**, 1505–1514 (2002).

80. Harscher, A. Elektronenholographie biologischer Objekte: Grundlagen und Anwendungsbeispiele. (University of Tubingen, 1999).

81. Frabboni, S., Matteucci, G., Pozzi, G. & Vanzi, M. Electron holographic observations of the electrostatic field associated with thin reverse-biased p-n junctions. *Phys. Rev. Lett.* **55**, 2196–2199 (1985).

82. Rau, W. D., Schwander, P., Baumann, F. H., Höppner, W. & Ourmazd, A. Two-dimensional mapping of the electrostatic potential in transistors by electron holography. *Phys. Rev. Lett.* **82**, 2614–2617 (1999).

83. Gribelyuk, M. A. *et al.* Mapping of Electrostatic Potential in Deep Submicron CMOS Devices by Electron Holography. *Phys. Rev. Lett.* **89**, 2–5 (2002).

84. Ravikumar, V., Rodrigues, R. P. & Dravid, V. P. Direct imaging of spatially varying potential and charge across internal interfaces in solids. *Phys. Rev. Lett.* **75**, 4063–4066 (1995).

85. Zhang, X., Hashimoto, T. & Joy, D. C. Electron holographic study of ferroelectric domain walls. *Appl. Phys. Lett.* **60**, 784–786 (1992).

86. Lichte, H. Are Ferroelectric Crystals Blaze-Gratings for Electrons.pdf. *Cryst. Res. Technol.* **35**, 887–898 (2000).

87. Park, J. B. *et al.* Impact of electron irradiation on electron holographic potentiometry. *Appl. Phys. Lett.* **105**, (2014).

88. Suzuki, H., Akase, Z., Niitsu, K., Tanigaki, T. & Shindo, D. Secondary electron effect on electron beam induced charging of SiO_2 particle analyzed by electron holography. *Microscopy* **66**, 167–171 (2017).

89. McCartney, M. R. Characterization of charging in semiconductor device materials by electron holography. *J. Electron Microsc. (Tokyo).* **54**, 239–242 (2005).

90. Gabor, D. A new microscopic principle. *Nature* **161**, 777–778 (1948).

91. Gabor, D. Microscopy by reconstructed Wave Fronts: II. *Proc. Phys. Soc.* **64**, 449–469 (1951).

92. Gabor, D. Nobel Lecture: Holography, 1948-1971. in *Nobel Lectures in Physics 1971-1980* (ed. Lundqvist, S.) (World Scientific Publishing Co., 1992).

93. Gabor, D. Microscopy by reconstructed wave fronts: II. *Proc. Phys. Soc. Sect. B* **64**, 449–469 (1951).

94. Haine, M. E. & Dyson, J. A modification to Gabor's proposed diffraction microscope. *Nature* **166**, 315–316 (1950).

95. DeVelis, J. B., Parrent, G. B. & Thompson, B. J. Image Reconstruction with Fraunhofer Holograms*. *J. Opt. Soc. Am.* **56**, 423 (1966).

96. Ross, F. M. & Stobbs, W. M. A study of the initial stages of oxidation of silicon using the Fresnel method. *Philisophical Mag. A* **63**, 1–36 (1991).

97. Xu, W., Jericho, M. H., Meinertzhagen, I. A. & Kreuzer, H. J. Digital in-line holography of microspheres. *Appl. Opt.* **41**, 5367 (2002).

98. Xu, W., Jericho, M. H., Meinertzhagen, I. A. & Kreuzer, H. J. Digital in-line holography for biological applications. *Proc. Natl. Acad. Sci. U. S. A.* **98**, 11301–11305 (2001).

99. Mazumdar, Y. C., Smyser, M. E., Heyborne, J. D., Slipchenko, M. N. & Guildenbecher, D. R. Megahertz-rate shock-wave distortion cancellation via phase conjugate digital in-line holography. *Nat. Commun.* **11**, 1–10 (2020).

100. Arienti, M. *et al.* Comparison of simulation and experiments for multimode aerodynamic breakup of a liquid metal column in a shock-induced cross-flow. *Phys. Fluids* **31**, (2019).

101. Guizar-sicairos, M. & Thibault, P. Ptychography: A solution to the phase problem. *Physics Today* **74**, 42–48 (2021).

102. Cowley, J. M. Twenty forms of electron holography. *Ultramicroscopy* **41**, 335–348 (1992).

103. Leith, E. N. & Upatnieks, J. Wavefront Reconstruction with Continuous-Tone Objects. *J. Opt. Soc. Am.* **53**, 1377 (1963).

104. Midgley, P. A. A. An introduction to off-axis electron holography. *Micron* **32**, 167–184 (2001).

105. Van Dyck, D. Through object electron holography. *J. Electron Microsc. (Tokyo).* **48**, 33–34 (1999).

106. Hasselbach, F. Progress in electron- and ion-interferometry. *Reports Prog. Phys.* **73**, (2010).

107. Lichte, H. Electron holography: Optimum position of the biprism in the electron microscope. *Ultramicroscopy* **64**, 79–86 (1996).

108. Joy, D. C. *et al.* Practical aspects of electron holography. *Ultramicroscopy* **51**, 1–14

(1993).

109. Tonomura, A. Electron-holographic interference microscopy. *Adv. Phys.* **41**, 59–103 (1992).

110. Prigent, M. & Morin, P. Charge effect in point projection images of carbon and collagen fibers. *J. Microsc.* **199**, 197–207 (2000).

111. Cumings, J., Zettl, A. & McCartney, M. R. Carbon nanotube electrostatic biprism: Principle of operation and proof of concept. *Microsc. Microanal.* **10**, 420–424 (2004).

112. Oshima, C., Rokuta, E. & Cho, B. Highly coherent electrons emitted from nano-scaled areas. *Chinese J. Phys.* **43**, 145–153 (2005).

113. *Modern Techniques for Characterizing Magnetic Materials*. (Springer, 2005).

114. Aharonov, Y. & Bohm, D. Significance of Electromagnetic Potentials in the Quantum Theory. *Phys. Rev.* **115**, 485–491 (1959).

115. Scherzer, O. The theoretical resolution limit of the electron microscope. *J. Appl. Phys.* **20**, 20–29 (1949).

116. Lichte, H. Optimum Focus for Taking Electron Holograms. *Ultramicroscopy* **38**, 13–22 (1991).

117. Lehmann, M. & Lichte, H. Tutorial on Off-Axis Electron Holography. *Microsc. Microanal.* **8**, S1431927602029938 (2002).

118. Lichte, H. Performance limits of electron holography. *Ultramicroscopy* **108**, 256–262 (2008).

119. Harscher, A. & Lichte, H. Experimental study of amplitude and phase detection limits in electron holography. *Ultramicroscopy* **64**, 57–66 (1996).

120. Lichte, H., Herrmann, K.-H. & Lenz, F. Electron noise in off-axis image plane holography. *Optik (Stuttg).* **3**, 135–140 (1987).

121. Lichte, H. Electron Holography: Phases matter. *J. Electron Microsc. (Tokyo).* **62**, 17–28 (2013).

122. Harscher, A. & Lichte, H. Experimental study of amplitude and phase detection limits in electron holography. *Ultramicroscopy* **64**, 57–66 (1996).

123. Kovács, A., Kasama, T., Mccartney, M. R. & David, J. *Springer Handbook of Microscopy chpt 16*. (2019).

124. de Ruijter, W. J., Weiss, J. K., De Ruijter ', W. J. & Weiss, J. K. Detection limits in quantitative off-axis electron holography. *Ultramicroscopy* **50**, 269–283 (1993).

125. Taniyama, A., Oikawa, T. & Shindo, D. Evaluation of the characteristics of a slow-scan CCD camera for a transmission electron microscope. *J. Electron Microsc. (Tokyo).* **48**, 257–260 (1999).

126. Born, M. *et al. Principles of Optics*. (Cambridge University Press, 1999). doi:10.1017/CBO9781139644181

127. Gabor, D. A New Microscope Principle. *Nature* 777–778 (1948).

128. Hÿtch, M. & Gatel, C. Phase detection limits in off-axis electron holography from pixelated detectors: Gain variations, geometric distortion and failure of reference-hologram correction. *Microscopy* **70**, 47–58 (2021).

129. Rice, W. J. *et al.* Routine determination of ice thickness for cryo-EM grids. *J. Struct. Biol.* **204**, 38–44 (2018).

130. Feja, B. & Aebi, U. Determination of the inelastic mean free path of electrons in vitrified

ice layers for on-line thickness measurements by zero-loss imaging. *J. Microsc.* **193**, 15–19 (1999).

131. Grimm, R., Typke, D., Bärmann, M. & Baumeister, W. Determination of the inelastic mean free path in ice by examination of tilted vesicles and automated most probable loss imaging. *Ultramicroscopy* **63**, 169–179 (1996).

132. Prieto, P., Quirós, C., Elizalde, E. & Sanz, J. M. Electron inelastic mean free path and dielectric properties of a-boron, a-carbon, and their nitrides as determined by quantitative analysis of reflection electron energy loss spectroscopy. *J. Vac. Sci. Technol. A Vacuum, Surfaces, Film.* **24**, 396–407 (2006).

133. Sadamatsu, S., Tanaka, M., Higashida, K. & Matsumura, S. Transmission electron microscopy of bulk specimens over 10μm in thickness. *Ultramicroscopy* **162**, 10–16 (2016).

134. Li, S., Chang, Y., Wang, Y., Xu, Q. & Ge, B. A review of sample thickness effects on high-resolution transmission electron microscopy imaging. *Micron* **130**, 102813 (2020).

135. Fujiyoshi, Y. Low Dose Techniques and Cryo-Electron Microscopy. in *Electron Crystallography of Soluble and Membrane Proteins: Methods and Protocols* (eds. Schmidt-Krey, I. & Cheng, Y.) 103–118 (Humana Press, 2013). doi:10.1007/978-1-62703-176-9_6

136. Gyobu, N. *Electron Crystallography of Soluble and Membrane Proteins*. *Human Press* (2013). doi:10.1007/978-1-62703-176-9_7

137. Cheng, Y., Grigorieff, N., Penczek, P. A. & Walz, T. A primer to single-particle cryo-electron microscopy. *Cell* **161**, 438–449 (2015).

138. Grant, T. & Grigorieff, N. Measuring the optimal exposure for single particle cryo-EM using a 2.6 Å reconstruction of rotavirus VP6. *Elife* **4**, 1–19 (2015).

139. Lichte, H. Electron holography approaching atomic resolution. *Ultramicroscopy* **20**, 293–304 (1986).

140. Linck, M., Lichte, H. & Lehmann, M. Off-axis electron holography: Materials analysis at atomic resolution. *Int. J. Mater. Res.* **97**, 890–898 (2006).

141. Linck, M., Freitag, B., Kujawa, S., Lehmann, M. & Niermann, T. State of the art in atomic resolution off-axis electron holography. *Ultramicroscopy* **116**, 13–23 (2012).

142. Friedrich, H., Frederik, P. M., De With, G. & Sommerdijk, N. A. J. M. Imaging of self-assembled structures: Interpretation of TEM and Cryo-TEM images. *Angew. Chemie - Int. Ed.* **49**, 7850–7858 (2010).

143. Dunin-Borkowski, R. E., McCartney, M. R., Kardynal, B. & Smith, D. J. Magnetic interactions within patterned cobalt nanostructures using off-axis electron holography. *J. Appl. Phys.* **84**, 374–378 (1998).

144. He, K., Cho, J. H., Jung, Y., Tom Picraux, S. & Cumings, J. Silicon nanowires: Electron holography studies of doped p-n junctions and biased Schottky barriers. *Nanotechnology* **24**, (2013).

145. Naydenova, K., Jia, P. & Russo, C. J. Cryo-EM with sub–1 Å specimen movement. *Science (80-.).* **370**, 223–226 (2020).

146. Egelman, E. H. The Current Revolution in Cryo-EM. *Biophys. J.* **110**, 1008–1012 (2016).

147. Kampjut, D., Steiner, J. & Sazanov, L. A. Cryo-EM grid optimization for membrane proteins. *iScience* **24**, 1–13 (2021).

148. Glaeser, R. M. Proteins, interfaces, and cryo-EM grids. *Curr. Opin. Colloid Interface Sci.* **34**, 1–8 (2018).

149. Russo, C. J. & Passmore, L. A. Ultrastable gold substrates: Properties of a support for high-resolution electron cryomicroscopy of biological specimens. *J. Struct. Biol.* **193**, 33–44 (2016).

150. Russo, C. J. & Passmore, L. A. Ultrastable gold subtrates for electron cryomiscroscopy. *Science (80-.).* **346**, 1377–1381 (2014).

151. Park, I. S., Kim, D. K., Adanyi, N., Varadi, M. & Kim, N. Development of a direct-binding chloramphenicol sensor based on thiol or sulfide mediated self-assembled antibody monolayers. *Biosens. Bioelectron.* **19**, 667–674 (2004).

152. Ansar, S. M. *et al.* Determination of the binding affinity, packing, and conformation of thiolate and thione ligands on gold nanoparticles. *J. Phys. Chem. C* **115**, 653–660 (2011).

153. Subramanian, V., Wolf, E. E. & Kamat, P. V. Catalysis with TiO2/Gold Nanocomposites. Effect of Metal Particle Size on the Fermi Level Equilibration. *J. Am. Chem. Soc.* **126**, 4943–4950 (2004).

154. Zhang, B., Chen, J., Cao, Y., Chai, O. J. H. & Xie, J. Ligand Design in Ligand-Protected Gold Nanoclusters. *Small* **17**, 2004381 (2021).

155. Dubochet, J. *et al.* Cryo-electron microscopy of vitrified specimens. *Q. Rev. Biophys.* **21**, 129–228 (1988).

156. Taylor, K. A. & Glaeser, R. M. Retrospective on the early development of cryoelectron microscopy of macromolecules and a prospective on opportunities for the future. *J. Struct. Biol.* **163**, 214–223 (2008).

157. Park, J. E., Lee, Y. & Nam, J. M. Precisely Shaped, Uniformly Formed Gold Nanocubes with Ultrahigh Reproducibility in Single-Particle Scattering and Surface-Enhanced Raman Scattering. *Nano Lett.* **18**, 6475–6482 (2018).

158. Sonnefeld, J. Surface charge density on spherical silica particles in aqueous alkali chloride solutions - Part 2. Evaluation of the surface charge density constants. *Colloid Polym. Sci.* **273**, 932–938 (1995).

159. Hiemstra, T. & Van Riemsdijk, W. H. A surface structural approach to ion adsorption: The charge distribution (CD) model. *J. Colloid Interface Sci.* **179**, 488–508 (1996).

160. Larson, I. & Attard, P. Surface charge of silver iodide and several metal oxides. Are all surfaces nernstian? *J. Colloid Interface Sci.* **227**, 152–163 (2000).

161. Brown, M. A., Bossa, G. V. & May, S. Emergence of a Stern Layer from the Incorporation of Hydration Interactions into the Gouy-Chapman Model of the Electrical Double Layer. *Langmuir* **31**, 11477–11483 (2015).

162. Brown, M. A., Goel, A. & Abbas, Z. Effect of Electrolyte Concentration on the Stern Layer Thickness at a Charged Interface. *Angew. Chemie - Int. Ed.* **55**, 3790–3794 (2016).

163. Cheng, D., Mitchell, D., Shieh, D. & Braet, F. Practical Considerations in the Successful Preparation of Specimens for Thin-Film Cryo-Transmission Electron Microscopy. *Curr. Microsc. Contrib. to Adv. Sci. Technol.* 880–890 (2012).

164. Weissenberger, G., Henderikx, R. J. M. & Peters, P. J. Understanding the invisible hands of sample preparation for cryo-EM. *Nat. Methods* **18**, 463–471 (2021).

165. Dubochet, J. The Physics of Rapid Cooling and Its Implications for Cryoimmobilization of Cells. *Methods Cell Biol.* **2007**, 7–21 (2007).

166. Tulk, C. A., Molaison, J. J., Makhluf, A. R., Manning, C. E. & Klug, D. D. Absence of amorphous forms when ice is compressed at low temperature. *Nature* **569**, 542–545 (2019).

167. Elsaesser, M. S., Winkel, K., Mayer, E. & Loerting, T. Reversibility and isotope effect of the calorimetric glass → liquid transition of low-density amorphous ice. *Phys. Chem. Chem. Phys.* **12**, 708–712 (2010).

168. Seidl, M. *et al.* Volumetric study consistent with a glass-to-liquid transition in amorphous ices under pressure. *Phys. Rev. B* **83**, 6–9 (2011).

169. Johari, G. P. Liquid state of low-density pressure-amorphized ice above its Tg. *J. Phys. Chem. B* **102**, 4711–4714 (1998).

170. McLeod, R. DM3 Import for Gatan Digital Micrograph. (2022).

171. McCartney, M. R. & Smith, D. J. Electron holography: Phase imaging with nanometer resolution. *Annu. Rev. Mater. Res.* **37**, 729–767 (2007).

172. Ishizuka, K. Optimized sampling schemes for off-axis holography. *Ultramicroscopy* **52**, 1–5 (1993).

173. Zhao, Z. *et al.* Robust 2D phase unwrapping algorithm based on the transport of intensity equation. *Meas. Sci. Technol.* **30**, 015201 (2018).

174. Xu, W. & Gumming, L. A region-growing algorithm for InSAR phase unwrapping. *IEEE Trans. Geosci. Remote Sens.* **37**, 124–134 (1999).

175. Quiroga, J. A. & Bernabeu, E. Phase-unwrapping algorithm for noisy phase-map processing. *Appl. Opt.* **33**, 6725 (1994).

176. Shindo, D. & Murakami, Y. Electron holography of magnetic materials. *J. Phys. D. Appl.*

Phys. **41**, (2008).

177. He, K., Ma, F. X., Xu, C. Y. & Cumings, J. Mapping magnetic fields of Fe3O4 nanosphere assemblies by electron holography. *J. Appl. Phys.* **113**, 1–4 (2013).

178. Thomas, J. M., Simpson, E. T., Kasama, T. & Dunin-Borkowski, R. E. Electron holography for the study of magnetic nanomaterials. *Acc. Chem. Res.* **41**, 665–674 (2008).

179. Signoretti, S. Electron holography for the analysis of magnetic and electric microfields in nanostructured systems. *Thesis* (Swiss Federal Institute of Technologry Zurich, 2003).

180. Cumings, J., Zettl, A., McCartney, M. R. & Spence, J. C. H. Electron holography of field-emitting carbon nanotubes. *Phys. Rev. Lett.* **88**, 568041–568044 (2002).

181. Sellner, B. & Kathmann, S. M. A matter of quantum voltages. *J. Chem. Phys.* **141**, (2014).

182. Wanner, M., Bach, D., Gerthsen, D., Werner, R. & Tesche, B. Electron holography of thin amorphous carbon films: Measurement of the mean inner potential and a thickness-independent phase shift. *Ultramicroscopy* **106**, 341–345 (2006).

183. Wolf, G., Gross, G. & Hayslip, I. C. Electrical Conductivity and Relaxation in Ice Crystals with Known Impurity Content. *J. Glaciol.* **21**, 143–160 (1978).

184. Truffer, M. Ice Physics. (2013). doi:10.1088/0031-9112/37/5/023

185. Russo, C. J. & Henderson, R. Charge accumulation in electron cryomicroscopy. *Ultramicroscopy* **187**, 43–49 (2018).

186. Hettler, S. *et al.* Charging of carbon thin films in scanning and phase-plate transmission electron microscopy. *Ultramicroscopy* **184**, 252–266 (2018).

187. Russo, C. J. & Henderson, R. Microscopic charge fluctuations cause minimal contrast loss in cryoEM. *Ultramicroscopy* **187**, 56–63 (2018).

188. Downing, K. H., McCartney, M. R. & Glaeser, R. M. Experimental characterization and mitigation of specimen charging on thin films with one conducting layer. *Microsc. Microanal.* **10**, 783–789 (2004).

189. Brink, J., Sherman, M. B., Berriman, J. & Chiu, W. Evaluation of charging on macromolecules in electron cryomicroscopy. *Ultramicroscopy* **72**, 41–52 (1998).

190. Cazaux, J. Correlations between ionization radiation effects in transmission electron. *Ultramicroscopy* **60**, 41–425 (1995).

191. Kilic, M. S., Bazant, M. Z. & Ajdari, A. Steric effects in the dynamics of electrolytes at large applied voltages. I. Double-layer charging. *Phys. Rev. E - Stat. Nonlinear, Soft Matter Phys.* **75**, 1–16 (2007).

192. Kilic, M. S., Bazant, M. Z. & Ajdari, A. Steric effects in the dynamics of electrolytes at large applied voltages. II. Modified Poisson-Nernst-Planck equations. *Phys. Rev. E - Stat. Nonlinear, Soft Matter Phys.* **75**, 1–11 (2007).

193. Behrens, S. H. & Grier, D. G. The Charge of Glass and Silica Surfaces. *J. Chem. Physicsournal Chem. Phys.* **115**, 6716 (2001).

194. Levin, Y., Dos Santos, A. P. & Diehl, A. Ions at the air-water interface: An end to a hundred-year-old mystery? *Phys. Rev. Lett.* **103**, 1–4 (2009).

195. Leung, K. Surface potential at the air-water interface computed using density functional theory. *J. Phys. Chem. Lett.* **1**, 496–499 (2010).

196. Pierson, J. *et al.* Improving the technique of vitreous cryo-sectioning for cryo-electron tomography: Electrostatic charging for section attachment and implementation of an anti-contamination glove box. *J. Struct. Biol.* **169**, 219–225 (2010).

197. Matatyaho Ya'Akobi, A. & Talmon, Y. Extending Cryo-EM to Nonaqueous Liquid Systems. *Acc. Chem. Res.* **54**, 2100–2109 (2021).

198. Gyobu, N. *et al.* Improved specimen preparation for cryo-electron microscopy using a symmetric carbon sandwich technique. *J. Struct. Biol.* **146**, 325–333 (2004).

199. Lagarias, J. C., Reeds, J. A., Wright, M. H. & Wright, P. E. Convergence properties of the Nelder-Mead simplex method in low dimensions. *SIAM J. Optim.* **9**, 112–147 (1998).

200. Li, H.-K. *et al.* Imaging Arrangements of Discrete Ions at Liquid–Solid Interfaces. *Nano Lett.* **20**, 7927–7932 (2020).

201. Rose, A. Television Pickup Tubes and the Problem of Vision. *Adv. Electron. Electron Phys.* **1**, 131–166 (1948).

202. Ichikawa, S. *et al.* Mean Inner Potential of Nanostructured Noble Metal Catalysts - Pt/TiO2 Catalyst -. *MRS Online Proc. Libr.* **788**, 821 (2004).

203. Zhang, X. & Oshima, Y. Reproducible measurement of the mean inner potential of gold nanoparticles using TIE method. in **1**, 0–1 (2013).

204. Iakoubovskii, K., Mitsuishi, K., Nakayama, Y. & Furuya, K. Mean free path of inelastic electron scattering in elemental solids and oxides using transmission electron microscopy: Atomic number dependent oscillatory behavior. *Phys. Rev. B - Condens. Matter Mater. Phys.* **77**, 1–7 (2008).

205. Smirnov, P. R., Grechin, O. V. & Trostin, V. N. Concentration dependence of the structure of aqueous solutions of lutetium nitrate according to X-ray diffraction. *Russ. J. Phys. Chem. A* **88**, 250–253 (2014).

206. Grechin, O. V., Smirnov, P. R. & Trostin, V. N. An X-ray diffraction study of aqueous

solutions of lutetium trichloride. *J. Struct. Chem.* **55**, 61–66 (2014).

207. López-González, H., Jiménez-Reyes, M., Solache-Ríos, M. & Rojas-Hernández, A. Solubility and hydrolysis of lutetium at different [Lu3+] initial. *J. Radioanal. Nucl. Chem.* **274**, 103–108 (2007).

208. Gittings, M. R. & Saville, D. A. The determination of hydrodynamic size and zeta potential from electrophoretic mobility and light scattering measurements. *Colloids Surfaces A Physicochem. Eng. Asp.* **141**, 111–117 (1998).

209. Instruments, M. Zeta potential: An Introduction in 30 minutes. *Zetasizer Nano Serles Tech. Note. MRK654-01* **2**, 1–6 (2011).

210. Suzuki, T. *et al.* Improvement of the accuracy of phase observation by modification of phase-shifting electron holography. *Ultramicroscopy* **118**, 21–25 (2012).

211. Lichte, H., Geiger, D. & Linck, M. Off-axis electron holography in an aberration-corrected transmission electron microscope. *Philos. Trans. R. Soc. A Math. Phys. Eng. Sci.* **367**, 3773–3793 (2009).